University of South Bohemia in České Budějovice
Faculty of Science

Deposition of functional thin films by plasma processes

Master thesis

Bc. Petr Sezemský

Supervisor: doc. RNDr. Vítězslav Straňák, Ph.D.

České Budějovice 2016

Sezemský, P., 2016: Deposition of functional thin films by plasma processes. Mgr. Thesis, in English. – 68 p., Faculty of Science, University of South Bohemia, České Budějovice, Czech Republic.

Annotation:
An aim of this work is a research of a deposition process of indium tin oxide by plasma assisted methods. The thesis deals with plasma diagnostics, e.g. Langmuir probe diagnostics and optical emission spectroscopy, as well as describes experiments of film deposition including their diagnostics, e.g. absorption spectroscopy, X-ray diffractometry and atomic force microscopy.

I hereby declare that the submitted master thesis has been written solely by me, only with use of sources and literature fully documented in a list of references.

I hereby declare that, in accordance with Article 47b of Act No. 111/1998 in the valid wording, I agree with the publication of my bachelor / master thesis, in full / in shortened form resulting from deletion of indicated parts to be kept in the Faculty of Science archive, in electronic form in publicly accessible part of the STAG database operated by the University of South Bohemia in České Budějovice accessible through its web pages.

Further, I agree to the electronic publication of the comments of my supervisor and thesis opponents and the record of the proceedings and results of the thesis defence in accordance with aforementioned Act No. 111/1998. I also agree to the comparison of the text of my thesis with the Theses.cz thesis database operated by the National Registry of University Theses and a plagiarism detection system.

České Budějovice, 14.12. 2016

_____

Petr Sezemský

ACKNOWLEDGEMENTS

First and foremost, I would like to thank my supervisor, doc. RNDr. Vítězslav Straňák, Ph.D., for giving me the chance to be involved in his research team and for his excellent guidance and insightful comments.

Finally, I want to thank my wife and my parents for their constant support which enabled my study.

Content

1 Introduction

An aim of this work is a research of a deposition process of transparent electrically conductive films prepared by plasma based methods. As a material was chosen Indium Tin Oxide for its uniquely high electrical conductivity and high transparency. The films were prepared by magnetron sputtering source, which is one of physical vapor deposition techniques typically used for industrial preparation of this particular material. The purpose of the research is development of novel type biosensors based on optical fibres coated by functional thin films. Such type of biosensors represents a new family of sensors with large application potential in bio-science with possibility to detect and interact only with defined group of organic molecules. In many biochemical applications, the use of small sensors to test a fluid with a volume of micro-and nanolitres is required because it is often practically impossible or very costly to obtain a larger volume of the tested fluid. Hence, development of new synthesis process that would enable to obtain a new class of optoelectronic sensors is a challenge in material science. The optoelectronic sensors have a big advantage since they combine two complementary features: an optical and electrical activity. Furthermore, such sensors can be easily functionalized with organic bio-film capable of simultaneous optical and electrochemical measurements. Hence, the combination of these two optical and electrochemical systems within one sensing structure allows selective detection and multi-parameter analysis of bio-analytes reaching sensor surface.

The thesis includes plasma diagnostics, e.g. Langmuir probe diagnostics and optical emission spectroscopy, as well as description of deposited film and their diagnostics, e.g. absorption spectroscopy, X-ray diffractometry and atomic force microscopy.

The following chapter brings brief introduction to commonly used surface engineering methods. It primarily focuses on plasma methods of thin film preparation and basics facts about low temperature plasma physics. The chapters 3 and 4 describe used diagnostical methods and experimental facility. The chapter 5 depict experimental setup and presents obtained results of plasma diagnostic and characterisation of thin films, respectively. All results are discussed together with the aim to bring deeper understanding of the film formation and optimization of the deposition process.

2 Surface engineering

Surface engineering involves modification of surface properties and near-surface region in a desirable way. It can involve a deposition process or a surface modification process. In deposition processes a material is added to the top of the underlying material (substrate) which is covered and not detectable externally. A surface modification process changes its properties while the substrate bulk material is unchanged.

Each process has its advantages, disadvantages, and applications. In some cases, surface modification processes can be used to modify the substrate surface prior to depositing a film or coating. For example, a steel surface can be hardened by plasma nitriding (ionitriding) prior to the deposition of a hard coating by a physical vapor deposition process. In other cases, a surface modification process can be used to change the properties of a coating.

An atomistic deposition is a one method during which material is deposited atom by atom. The resulting film can range from single crystal to amorphous, fully dense to less than fully dense, pure to composite, and thin to thick. Generally, the term "thin film" is applied to layers which have thicknesses on the order of a micron or less (1 micron = 10^{-6} m) and may be as thin as a few atomic layers [1]. Thicker deposits are typically called coatings. The term "thick film" is usually not used for thick atomistically deposited vacuum deposits as that term is used for "paint-on," types of deposition.

Often the properties of thin films are affected by the properties of the underlying material (substrate) and can vary through the thickness of the film. An atomistic deposition process can be done in a vacuum, plasma, gaseous, or electrolytic environment [1].

2.1 Methods for deposition of thin films and coatings for technological applications

This part brings short introduction to several techniques commonly used for deposition of thin films and coatings with special emphasis on the techniques, which use plasma.

Chemical Vapor Deposition

Thermal Chemical Vapor Deposition (CVD) (or vapor plating) is the deposition of atoms or molecules by the high temperature reduction or decomposition of a chemical vapor precursor containing the material to be deposited. Reduction is usually accomplished by hydrogen at an elevated temperature. Decomposition is achieved by thermal activation. The deposited material may react with other gases in the system to create compounds. Chemical vapor

deposition processing is generally accompanied by unused precursor and volatile reaction byproducts which are main reason for a novel techniques development [1].

Electroplating, Electroless Plating, and Displacement Plating

Electroplating is the deposition on the cathode of metallic ions from the electrolyte of an electrolysis cell. Only about 10 elements and some alloy composition are commercially deposited from aqueous solutions [1]. A thin film of material deposited by electroplating is often on the order of 1 μm thick [1]. Typically, the anode of the electrolytic cell is of the material being deposited and is consumed during the deposition process. In some cases, the anode material is not consumed and the material to be deposited comes only from the solution (e.g. chemical precursor), which must be continually replenished [1].

In electroless or autocatalytic plating, no external voltage/current source is required. The voltage/current is supplied by the chemical reduction of an agent at the deposit surface. The reduction reaction is catalyzed by a material, which is often boron or phosphorous.

Electrophoresis is based on the migration of charged particles in an electric field. The particles may be charged and non-soluble in the aqueous electrolyte. Alternatively, some of the components can be treated so that they are soluble in water but will chemically react near an electrode so their solubility is decreased [1].

Chemical Reduction

Some thin films can be deposited from chemical solutions at low temperatures by immersion in a two-part solution that gives a reduction reaction. “Chemical silvering” of mirrors and vacuum flasks is a common example [1].

The previous methods have severe disadvantages such as high costs of materials, high temperatures needed in process and use of dangerous chemicals, which can be solved by use of plasma-assisted deposition methods. For that reason, a novel methods of thin film deposition are looked for. A plasma based methods seems to be promising tools for deposition of wide range of materials.

Following part concerns basic physics of industrially used plasma.

2.2 Low temperature plasma

Plasma is a collection of free charged particles and electrically neutral particles moving in random directions with large average kinetic energy (0.1 eV – 10 eV per particle). Electrical plasma discharges have the following features:

1. they are driven electrically;
2. charged particle collisions with neutral gas molecules are important;
3. there are boundaries at which surface losses are important;
4. ionization of neutrals sustains the plasma in the steady state;
5. the electrons are not in thermal equilibrium with the ions.

A simple electrical discharge is shown schematically in figure 2-1. It consists of a voltage source that drives current through a low-pressure gas between two parallel conducting plates or electrodes. The gas form plasma, usually weakly ionized; the plasma density is only a small fraction of the neutral gas density [2].

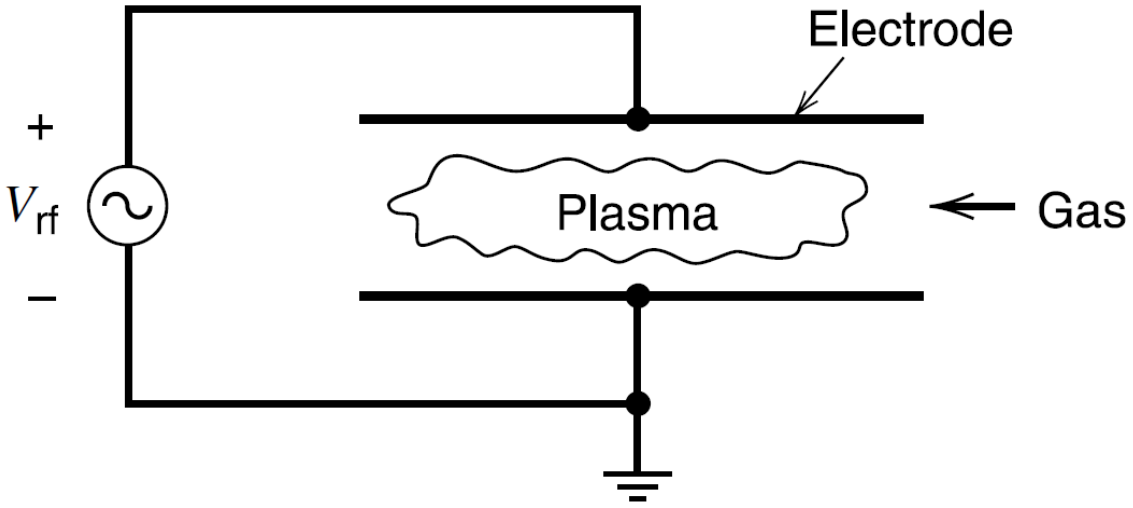

Figure 2-1 A simple discharge schematics [2].

Ionization degree of plasma

Ionization degree of plasma α indicates the ratio of ionized particles n_i to total particle number $n_i + n_n$ in plasma.

$$\alpha = \frac{n_i}{n_i + n_n} \qquad \text{Eq. 1}$$

Depending on the degree of ionization, two types of plasma can be distinguished:

- Weakly ionized plasma $\alpha \ll 1$ concentrations of neutral particles prevails over-charged
- Strongly ionized plasma $\alpha \leq 1$ concentration of charged particles prevails over neutral

The electrical conductivity of plasma

Unlike gas, plasma contains free electric charges, and therefore is electrically conductive. The electrical conductivity of plasma is one of the most important physical properties, which makes it suitable for various technical applications. Plasma electrical conductivity greatly depends on the plasma ionization degree. In the first case the electrical conductivity of the plasma increases with the concentration of charged particles. With a constant density of the charged particle, electric conductivity of the plasma decreases with increasing temperature of electrons. For strongly ionized plasma, the situation is completely different: the electrical conductivity does not depend on the concentration of charged particles and increases with the electron temperature to the power 3/2. Therefore, plasma at high temperatures may be more conductive than metallic conductors. For example, hydrogen plasma at 100MK has 100 times greater electrical conductivity than pure copper at room temperature [3]. However, high temperature plasma is typically not as widely employed for film deposition as low-temperature. From this reason, further part focuses attention primarily to low-temperature plasma.

Quasi-neutrality

Plasma contains free charge carriers, but since the total charge of the negatively charged particle n_e is the same as the total charge of positively charged particles n_i, plasma behaves as electrically neutral.

$$n_e \cong n_i$$

In laboratory experiments, sometimes a plasma is used, which is not neutral, and may even be composed of only one type of charge.

Debye shielding radius

If no external electric field is applied, the concentration of electrons and ions are the same and equal to n_0. If stationary charge q is inserted into plasma, the electric field of the charge influence charged plasma particles: particles with the same charge will be repelled while particles with opposite

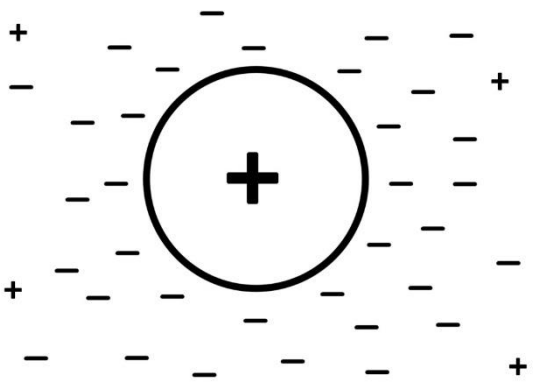

Figure 2-2 Shielding of charge inserted into plasma.

charge will be attracted, as shown in the figure 2-2. This plasma is polarized and will shield the electric field of the inserted charge. The assumption of homogeneous plasma shows spherically symmetrical distribution of charged particles near the inserted charge [3].

Generally, it is expected that ions are considered as stationary background due to their weight, which is much bigger than the mass of the electrons:
Starting from the Maxwell equation:

$$divD = \rho$$

can be substituted $D = \varepsilon_0 E$ and $E = -\nabla\varphi$ where ρ is the charge density, D is the electric induction, ε_0 is the permittivity of vacuum, E is the intensity of the electric field and $\nabla\varphi$ the gradient of electric potential. From these relations, a Poisson equation for electric potential follows:

$$\nabla^2\varphi = -\frac{\rho}{\varepsilon_0} = -e\frac{n_i - n_e}{\varepsilon_0}$$

$$n_i \approx n_0$$

Form Boltzmann distribution we obtain:

$$n_e = n_0 \cdot \mathrm{e}^{\frac{e\varphi}{k_B T_e}}$$

n_0 is concentration in the area where the charge is shielded, k_B is the Boltzmann constant, T_e is the temperature of electrons, e is charge of electron

$$\nabla^2\varphi = -\frac{\rho}{\varepsilon_0} = -\frac{e}{\varepsilon_0}\left[n_0 - n_0 \cdot \mathrm{e}^{\frac{e\varphi}{k_B T_e}}\right] = -\frac{en_0}{\varepsilon_0}\left[1 - \mathrm{e}^{\frac{e\varphi}{k_B T_e}}\right]$$

According to Taylor series we can approximate $e^a \approx 1 + a$

$$\nabla^2\varphi = -\frac{en_0}{\varepsilon_0}\left[1 - 1 - \frac{e\varphi}{k_B T_e}\right]$$

$$\nabla^2\varphi = \frac{e^2 n_0}{\varepsilon_0 k_B T_e} \cdot \varphi$$

$$\frac{d^2\varphi}{d\boldsymbol{r}^2} = \frac{e^2 n_0}{\varepsilon_0 k_B T_e} \cdot \varphi$$

Using a substitution:

$$\frac{1}{\lambda_D^2} = \frac{e^2 n_0}{\varepsilon_0 k_B T_e}$$

we finally obtained a shielding radius

$$\lambda_D = \sqrt{\frac{\varepsilon_0 k_B T_e}{e^2 n_0}} \qquad \text{Eq. 2}$$

λ_D is frequently called as Debye shielding radius. This relationship fits good only for low-temperature plasma, where ions move slowly (compared to electron) that can be considered as stationary.

The final potential distribution has the following form:

$$\varphi(r) = \varphi_0 \cdot \mathrm{e}^{-\frac{r}{\lambda_D}} = \frac{Q_0}{4\pi\varepsilon_0 r} \cdot \mathrm{e}^{-\frac{r}{\lambda_D}} \qquad \text{Eq. 3}$$

φ_0 is inserted potential, Q_0 is inserted charge [3].

The number of particles in Debye layer is:

$$N_d = \frac{4\pi}{3} n_e \lambda_d^3 \qquad \text{Eq. 4}$$

Temperature of the plasma

Mean kinetic energy of particles in plasma is defined by:

$$E = \frac{3}{2} k_\mathrm{B} T_\mathrm{e,i} \quad \text{and} \quad E = \frac{1}{2} m_\mathrm{e,i} v_\mathrm{e,i}^2$$

From there:

$$\frac{3}{2} k_\mathrm{B} T_\mathrm{e,i} = \frac{1}{2} m_\mathrm{e,i} v_\mathrm{e,i}^2$$

$$T_\mathrm{e,i} = \frac{1}{3} \frac{m_\mathrm{e,i} v_\mathrm{e,i}^2}{k_\mathrm{B}} \qquad \text{Eq. 5}$$

Where $T_\mathrm{e,i}$ is the temperature of the electrons/ions, k_B is the Boltzmann constant, $m_\mathrm{e,i}$ is the mass of the electrons/ions, $v_\mathrm{e,i}^2$ is the mean square velocity of the electrons/ions.

$$[T] = \mathrm{eV}$$

$$1\mathrm{eV} \approx 11600\mathrm{K}$$

According to the temperature of plasma, two types of plasma can be distinguished:

- High temperature $T_\mathrm{e} \geq 100$ eV ($T_e \cong T_i$)
- Low temperature $T_\mathrm{e} < 100\ eV$ ($T_e > T_i$)

According to the temperature of electrons and ions, three types of plasma can be distinguished:

- The plasma in complete thermodynamic equilibrium (CTE) $T_e = T_i$
- The plasma in local thermodynamic equilibrium (LTE) $T_e = T_i$ in a small area
- The plasma out of thermodynamic equilibrium (non-LTE) $T_e \gg T_i$

Anisothermicity of the plasma

Anisothermicity of the plasma τ indicates the ratio of the electron temperature T_e to the temperature of ions T_i.

$$\tau = \frac{T_e}{T_i}$$

According to the anisothermicity, two types of plasma can be distinguished:

- Isothermal plasma $\tau = 1$
- Non-isothermal plasma $\tau \gg 1$

Advantages of using plasma in deposition processes

Plasma can be very beneficial for deposition of materials with high melting points, which is problematic or impossible for conventional methods. Composition of deposited films is close to that of the source material. Plasma deposited films typically have a better adhesion on the substrate. Plasma process can be run at room temperatures utilizing unique properties of plasma. Using plasma deposition can facilitate epitaxial growth and other advanced processes.

- Plasma deposited films are sometimes more corrosion resistant and harder than coatings applied by the electroplating process. Most layers are greatly resistant to abrasion and are so durable that protective topcoats are almost never necessary.
- With plasma deposition, it is possible to utilize practically any type of inorganic and some organic materials on equally diverse types of substrates and surfaces.
- Advanced plasma deposition methods allow to prepare composite material with required stoichiometry ratio.

2.3 Plasma deposition of thin films

Plasma-assisted deposition, implantation, and surface modification are important materials processes for production of films on surfaces and/or modifying their properties. For example, the cycle of film and mask deposition, mask patterning, implantation or other modification as etching, and mask stripping represents modern methods for fabrication of integrated circuit devices, for example. Because device structures are sensitive to temperature, high-temperature deposition processes cannot be used in many cases. Fortunately, due to the nonequilibrium nature of low-pressure processing discharges, films, which would need high temperature when deposited using other methods, can be prepared at low temperatures. Furthermore, films can be deposited with improved properties, nonequilibrium chemical compositions, and crystal morphologies that are unattainable under equilibrium deposition

conditions at any temperature. Unique films that are not of natural properties can be deposited by low temperature plasma, for example, Diamond-Like Carbon (DLC) films.

As an example, two methods for integrated circuit fabrication can be pointed out. Most aluminium thin films (i.e., Al/Cu or Al/Si) are deposited on the wafer by physical sputtering from an aluminium or alloy target; this is essentially a room-temperature process. Although thermal evaporation sources can be used, it is more difficult to control film uniformity and composition with these sources. Another example is the final insulating "capping" layer on many devices, silicon nitride, which is deposited by plasma-enhanced chemical vapor deposition at temperatures near 300° C. An equivalent chemical vapor deposition (CVD) would require temperatures near 900° C, and therefore cannot be used because it would melt the aluminium, destroying the device [1]. Furthermore, by varying the ion bombardment and other plasma parameters in plasma-enhanced chemical vapor deposition of silicon nitride, the film composition, stress, and integrity can be controlled, greatly increasing its reliability as a capping layer.

Following two methods depends on use of plasma discharge in the process.

Plasma-Enhanced Chemical Vapor Deposition (PECVD)

Plasma may be used in CVD reactors to "activate" and partially decompose the precursor or to enhance or even induce chemical reaction necessary for efficient film growth. This allows deposition at a temperature lower than thermal CVD and the process is called plasma-enhanced CVD (PECVD) or plasma-assisted CVD (PACVD). The plasma is typically generated by radio frequency (RF) techniques. Figure 2-3 shows a parallel plate CVD reactor that uses RF power to generate the plasma. This type of PECVD reactor is in common use in the semiconductor industry to deposit silicon nitride (Si_3N_4) and phosphosilicate glass (PSG), encapsulating layers a few microns thick with deposition rates of 5–100 nm/min [1]. At low pressures, concurrent energetic particle bombardment during deposition can affect the properties of films deposited by PECVD [1].

Plasma-based CVD may also be used to deposit polymer films (plasma polymerization). In this case the precursor vapor is a monomer that becomes crosslinked in the plasma and on the surface to form an organic or inorganic polymer film. These films have very low porosity and excellent surface coverage [1].

Chemical vapor deposition consists of a thermally activated set of gas-phase and surface reactions that create a solid product at a substrate. In PECVD, the gas phase and often the surface reactions are controlled or strongly modified by the plasma properties. In place of thermal activation in CVD, the critical initial step in PECVD is electron impact dissociation of the buffer process gas (usually Ar with another possible gases as oxygen or nitrogen). Since T_e ~ 2–5 eV in a low-pressure discharge, the electrons can easily initiate gas dissociation and ionization which can finally result in deposition which can be carried out at temperatures much lower than for CVD.

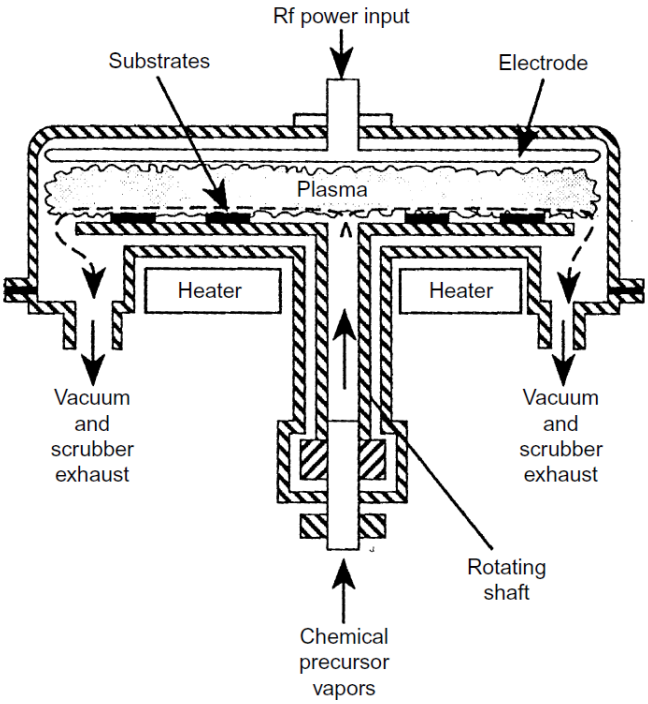

Figure 2-3 Parallel Plate Plasma-enhanced Chemical Vapor Deposition (PECVD) Reactor. Typical Parameters are: Radio Frequency (RF) – 50 kHz to 13.56 MHz; Temperature – 25 to 700 °C; Pressure – 10 Pa to 250 Pa; Gas flow rate – 200 sccm [1].

Because chemical reactions between neutral gas-phase precursor components are often required for PECVD, the discharge pressures used are in the range 10-100 Pa, considerably higher pressures than those used for plasma-assisted etching. The neutral mean free paths are therefore small, of order 0.003-0.3 mm [2]. The plasma densities are in the range 10^9-10^{11} cm^{-3}, and the fractional ionizations are low [2]. As for etching, the deposition is limited by either the gas flow rate and pressure or by the discharge power. Film properties such as composition, stress, and morphology can be in principle influenced by a substrate temperature *T*. Consequently, *T* is also usually optimized to achieve a desired set of film properties [2].

Deposited film uniformity is a critical issue for PECVD because of the high pressures, high flow rates, short mean free paths, high gas-phase reaction rates, and high surface sticking probabilities for some gas-phase deposition precursors (often, neutral radicals). This combination of factors makes it very difficult to achieve uniform precursor and ion fluxes

across the substrate area. Hence, great care is required in design of the neutral transport system for flow of gases into and out of the reaction zone. Similarly, the variation of the power deposition per unit area in the discharge must be carefully controlled. For these reasons, RF-driven parallel plate discharge geometries have been favoured, although some depositions have been performed using high-density cylindrical discharges, such as helicons, and RF inductive discharges (TCPs) [2].

It should be noted, however, that plasma-enhanced chemical vapor deposition cannot replace CVD in some applications; for example, most low-temperature plasma-enhanced chemical vapor deposition films are amorphous and not crystalline, which can more easily be achieved with CVD. Where high temperatures are allowed, CVD can be the method of choice for deposition of metals, dielectrics, and semiconducting films [1].

2.4 Physical Vapor Deposition

Physical vapor deposition processes (PVD), often just called thin film processes, are atomistic deposition processes in which material is vaporized from a solid or liquid source in the form of atoms or molecules and transported in the form of a vapor through a vacuum or low pressure gaseous (or plasma) environment to the substrate, where it condenses. Typically, PVD processes are used to deposit films with thicknesses in the range of a few nm to thousands of nm; however, they can also be used to form multilayer coatings, graded composition deposits, very thick deposits, and freestanding structures. The substrates can range in size from very small to very large. The substrates can range in shape from flat to complex geometries. Typical PVD deposition rates are 1-10 nm per second [1].

Physical vapor deposition processes can be used to deposit films of elements and alloys as well as compounds using reactive deposition processes. In reactive deposition processes, compounds are formed by the reaction of the depositing material with the ambient gas environment such as nitrogen (e.g. titanium nitride, TiN) or with a co-depositing material (e.g. titanium carbide, TiC and many others). Quasi-reactive deposition is the deposition of films of a compound material from a compound source where loss of the more volatile species or less reactive species during the transport and condensation process is compensated by having a partial pressure of reactive gas in the deposition environment; for example, the quasi-reactive sputter deposition of ITO (indium–tin oxide) from an ITO sputtering target using a partial pressure of oxygen in the plasma [1].

The main categories of PVD processing, vacuum deposition (evaporation), arc vapor deposition, and ion plating and sputter deposition will be briefly described in the following part. They are also depicted in figure 2-5.

Vacuum Deposition (Vacuum Evaporation)

Vacuum deposition, which is sometimes called vacuum evaporation, is a PVD process in which material from a thermal vaporization source travel to the substrate with little or no collision with molecules of the gas in the space between the source and substrate. Usually, vacuum deposition is performed in the gas pressure range of 10^{-3} to 10^{-7} Pa, providing the ability to reduce gaseous contamination in the deposition system [1]. Thermal evaporation is generally done employing thermally heated sources such as tungsten wire or high energy electron beam.

Vacuum deposition is used to form, for example, decorative coatings, mirror coatings, optical interference coatings, permeation barrier films on flexible packaging materials, electrically conductive films, corrosion protective coatings and wear resistant coatings.

Arc Vapor Deposition

Arc vapor deposition uses a high current, low voltage arc to vaporize a cathodic electrode (cathodic arc) or anodic electrode (anodic arc) to deposit the vaporized material onto a substrate. The vaporized material is usually highly ionized and the substrate is biased to accelerate the ions ("film ions") to the substrate surface.

Arc vapor deposition is used to deposit hard and decorative coatings. The ions ("film ions") that are formed in arc vaporization are useful in the ion plating process, too.

Ion Plating

Ion plating utilizes bombardment of the depositing film by atomic-sized energetic particles to control and modify the deposited film properties. The deposition material may be processed either by arc erosion, sputtering, evaporation, or by decomposition of a chemical vapor precursor.

By using a reactive gas in the plasma, films of compound materials can be deposited. Ion plating can provide dense coatings at relatively high gas pressures where gas scattering can enhance surface coverage.

Ion plating is used to deposit high density optical coatings, adherent metal coatings, hard coatings of compound materials and conformal coatings on complex surfaces.

Sputtering based Deposition

Sputtering deposition is the deposition of particles vaporized from a solid surface, so-called target, by the physical sputtering process. Physical sputtering is a non-thermal vaporization process where surface atoms of deposited material are physically ejected from a solid target by momentum transfer from an energetic bombarding particle, which are usually ions of gas, accelerated by plasma. This PVD process is sometimes just called sputtering. Generally, the source-to-substrate distance is short compared to vacuum deposition. Sputter deposition can be performed by energetic ion bombardment of a solid surface (sputtering target) in a vacuum using an ion gun or low pressure plasma (< 0.5 Pa) where the sputtered particles do not frequently collide with gas particles in the space between the target and the substrate [1].

Sputtering can also be done in a higher plasma pressure (0.5–4 Pa) where energetic particles, sputtered or reflected from the sputtering target, before they reach the substrate surface are "thermalized" by gas phase collisions [1]. The plasma used in sputtering can be confined near the sputtering surface or may fill the region between the source and the substrate. The sputtering source can be an element, alloy, mixture, or a compound material(s) which is evaporated from its surface. The sputtering target provides a long-lived vaporization source that can be mounted in any direction. Compound materials such as TiN and zirconium nitride (ZrN) are commonly called "reactively sputter deposited" because of reaction of sputtered metal atoms in a reactive atmosphere. The presence of the plasma "activates" the reactive gas ("plasma activation"), enhancing its chemical reactivity.

Sputtering has wide application in deposition of thin film, decorative coatings, reflective coatings, magnetic films, optical coatings, films for semiconductor and electronics industry, coatings on architectural glass, dry film lubricants, and hard coatings (used to protect tools, engine parts, etc.).

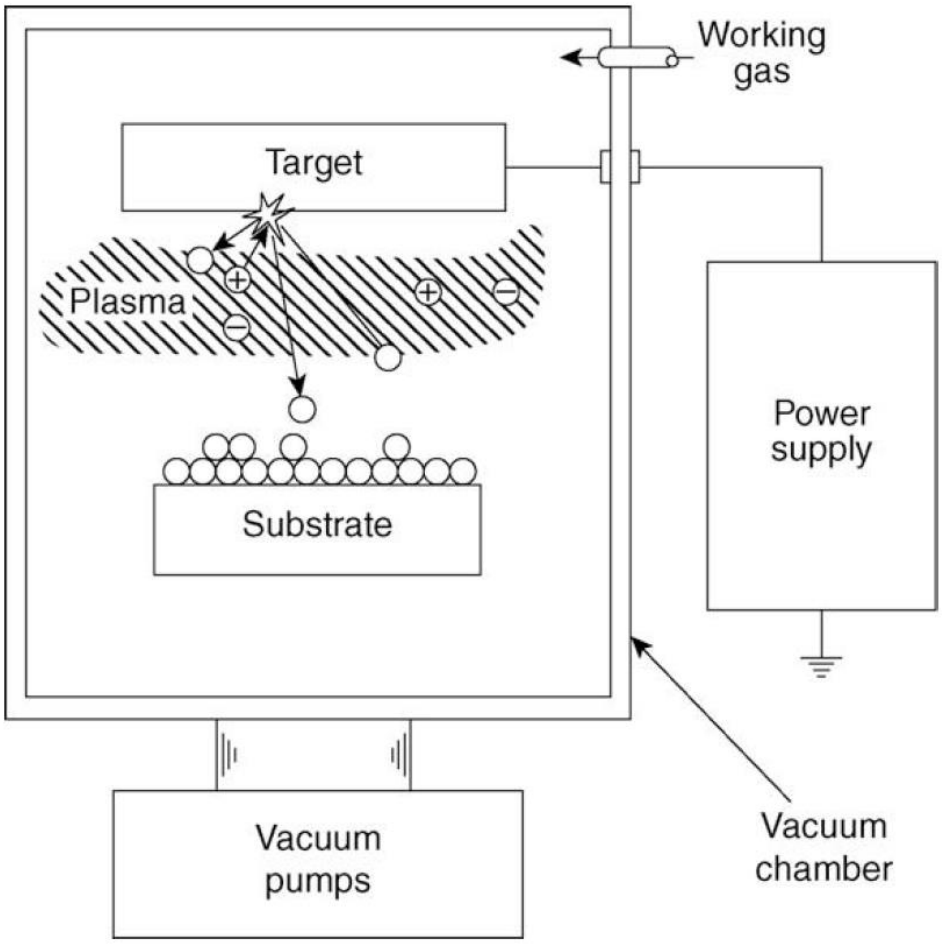

Figure 2-4 Simplified illustration of the sputtering deposition process. Positively charged particles (primarily of a working gas) are accelerated towards the target which is sputtered. The sputtered particles of the target condensate on a surface of a substrate, creating a film [4].

In the sputtering process, illustrated schematically in figure 2-4, positive gas ions (usually argon ions) produced in a glow discharge (gas pressure 2.5–20 Pa) bombard the target material (also called the cathode), providing sputtering to groups of atoms which then pass into the vapor phase and deposit onto the substrate [4].

Argon ions at 500–1000 V are usually used [2]. Because sputtering yields are of order unity for almost all metal target materials, a very wide variety of pure metals, alloys, and insulators can be deposited. Physical sputtering, especially of elemental targets, is a well understood process, enabling easy designed of the deposition process. Heat resistant materials can also be easily sputtered. Reasonable deposition rates with excellent film uniformity, good surface smoothness, and adhesion can be achieved over large areas [2].

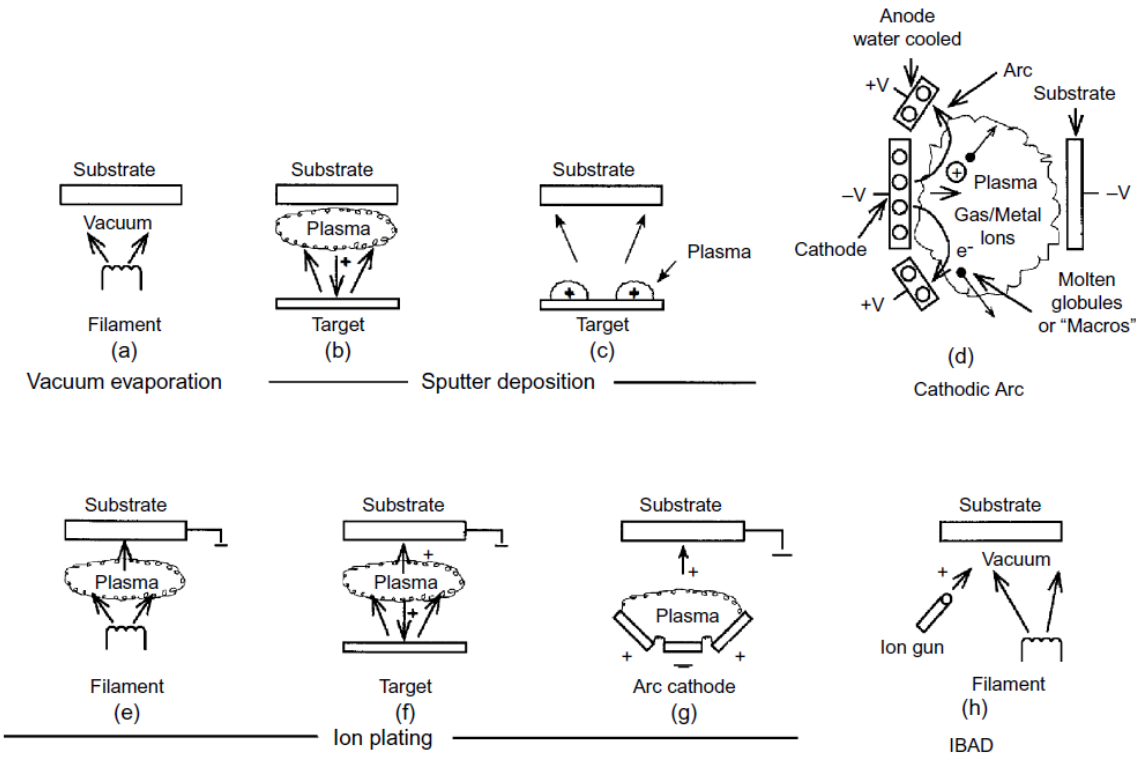

Figure 2-5 PVD Processing Techniques: (a) Vacuum Evaporation, (b) and (c) Sputter Deposition in a Plasma Environment, (d) Sputter Deposition in a Vacuum, (e) Ion Plating in a Plasma Environment with a Thermal Evaporation Source, (f) Ion Plating with a Sputtering Source, (g) Ion Plating with an arc Vaporization Source, and (h) Ion Beam-Assisted Deposition (IBAD) with a Thermal Evaporation Source and Ion Bombardment from an Ion Gun [1].

2.4.1 Magnetron – principle, features and benefits

The sputtering and evaporation of solid materials are fundamental physical processes currently used in the physical vapor deposition of thin films. Up to the mid-1970s, however, the evaporation dominated over the sputtering in PVD technologies. This was mainly due to a very low sputter deposition rate a_{Ds} (≪µm/min) of the film and relatively high pressures p (>1 Pa) needed to sustain the sputtering discharge. The breakthrough arrived in 1974 when the planar magnetron was discovered. From this moment, a very strong development of the sputtering method started [5].

Figure 2-6 The magnetron without target. Downloaded from [6].

Magnetron sputtering is a versatile plasma deposition method. Compared to the old method of diode sputtering the magnetron sputtering offers significantly higher deposition rates at lower sputtering pressures, reduced substrate heating and lower film contaminations. Today, magnetron sputtering is used for the deposition of a large variety of thin films:

- Metallic films,
- Oxide and nitride films,
- Infrared-reflective films for low emissivity coatings,
- Hard coatings [7].

In the following part the principles of magnetron sputtering are summarized.

Magnetron success is caused primarily by implementation of magnetic field in the deposition system.

Particles in crossed electric and magnetic field are influenced by a Lorentz force. The Lorentz force equation of motion for a particle of charge q (q = -e for electrons and n×e for n–times ionized atoms, e is the elementary charge), mass m, and velocity $\boldsymbol{v}$ in an electric field $\boldsymbol{E}$ and a magnetic field $\boldsymbol{B}$ is given by:

$$m\frac{d\boldsymbol{v}}{dt} = q(\boldsymbol{E} + \boldsymbol{v}\times\boldsymbol{B})$$

From there for $\boldsymbol{E}$=0 and $\boldsymbol{B}$≠0

$$\frac{d\boldsymbol{v}}{dt} = \frac{q\boldsymbol{v}\times\boldsymbol{B}}{m}$$

These particles will rotate around magnetic field lines in the plane perpendicular to the magnetic field lines with circular frequency:

$$\omega_c = \frac{qB}{m} \qquad \text{Eq. 6}$$

where *B* the magnetic field intensity.

In a magnetron, the electric and the magnetic field are locally perpendicular to each other. This cause the particle to drift with drifting velocity:

$$\boldsymbol{v_D} = \frac{\boldsymbol{E}\times\boldsymbol{B}}{B^2} \qquad \text{Eq. 7}$$

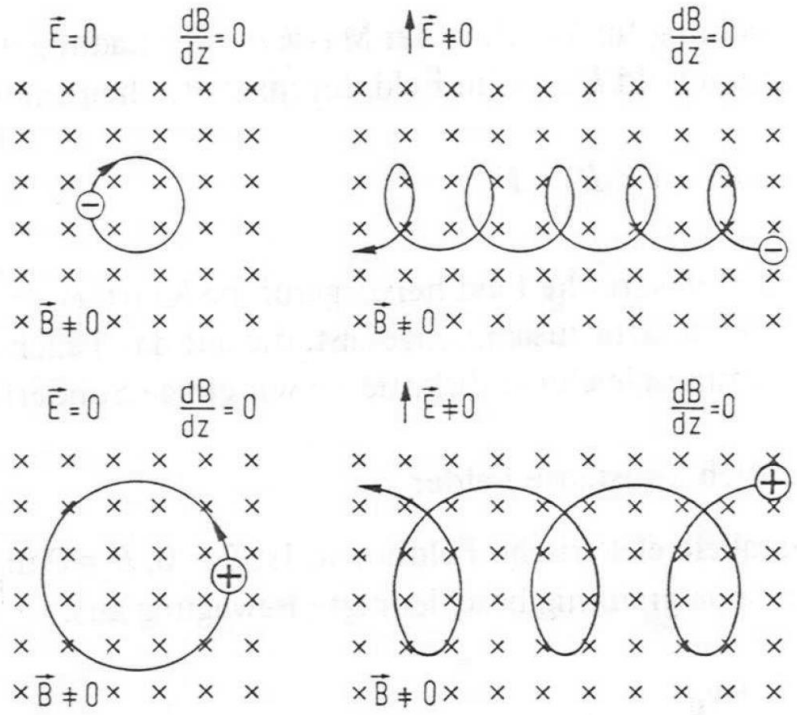

Figure 2-7 Examples of possible behaviour of charged particles in magnetic/electromagnetic field [7].

From technical point of view magnetron is a diode sputtering source which uses as an essential addition magnets behind the target (target represents a cathode made of material to be deposited) generating a magnetic field parallel (or at least locally parallel) to the cathode to form an electron trap as shown on figures 2-8 and 2-9. In this way, the discharge plasma is concentrated in front of the target surface as an endless (closed) toroidal ring bounded by a tunnel-shaped magnetic field. The most remarkable difference to a diode glow discharge is that a high current can be driven through the plasma at low pressures which is nearly independent of the voltage. The magnetron discharge excited by a direct current (DC) voltage is low pressure cold cathode discharges which is self-sustained by ion-induced

secondary electrons from the cathode. After acceleration in the cathode dark space these secondary electrons are called primary electrons which ionize the sputtering gas (typically argon) to produce gas ions that again after target bombardment release a further electron from the target.

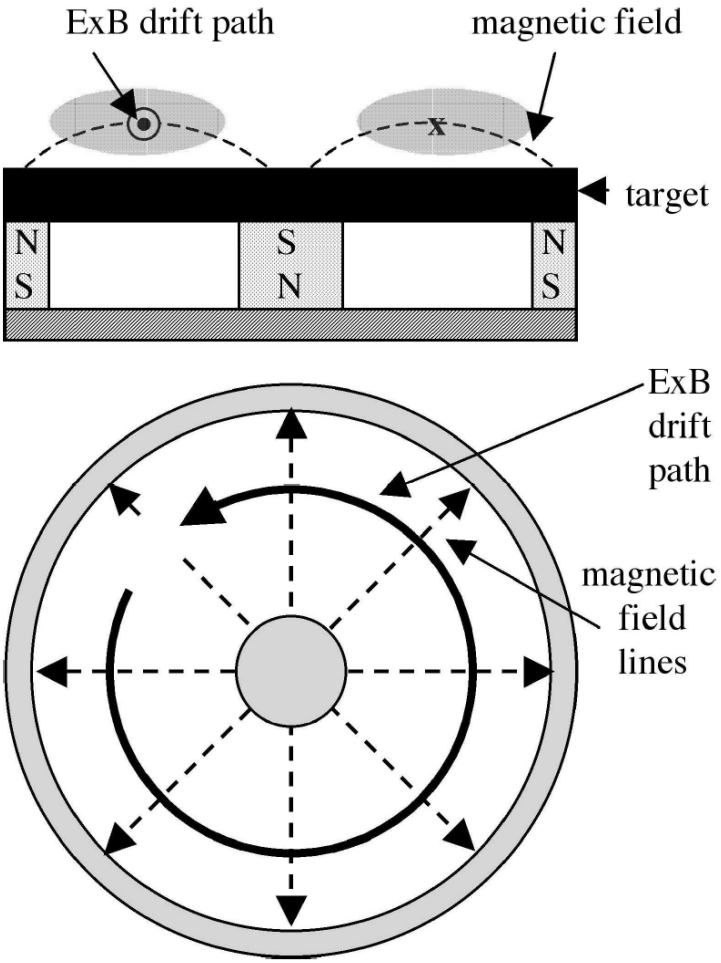

Figure 2-8 Representation of the magnetic field of magnetron and the drift path [7].

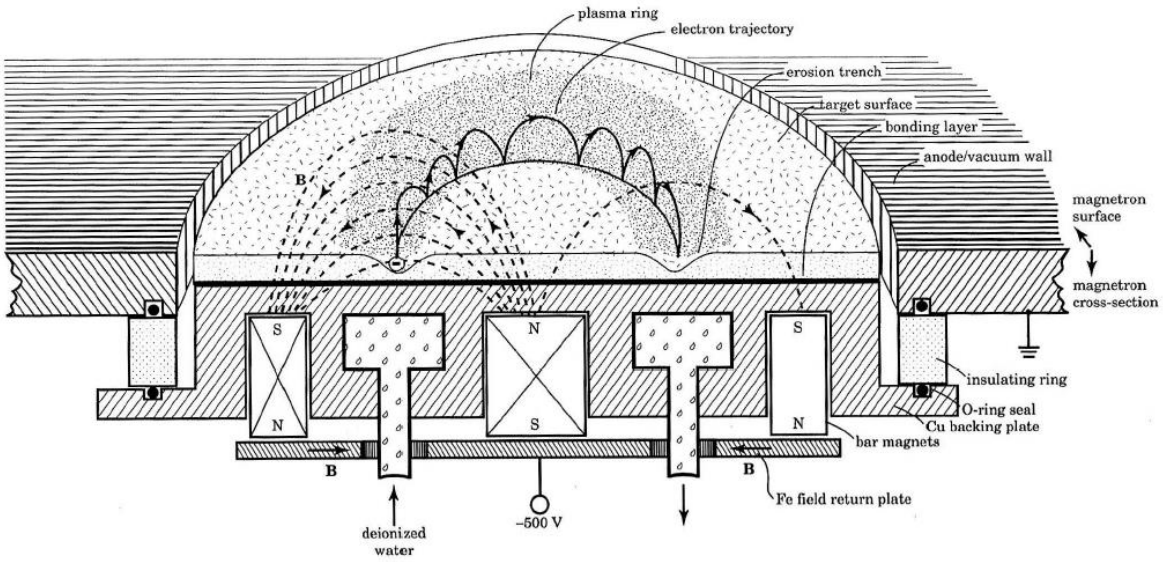

Figure 2-9 Scheme of a circular planar magnetron according to Smith. The magnetic field is depicted as dashed lines, while the cycloidal electron path is shown in larger size for clarity [7].

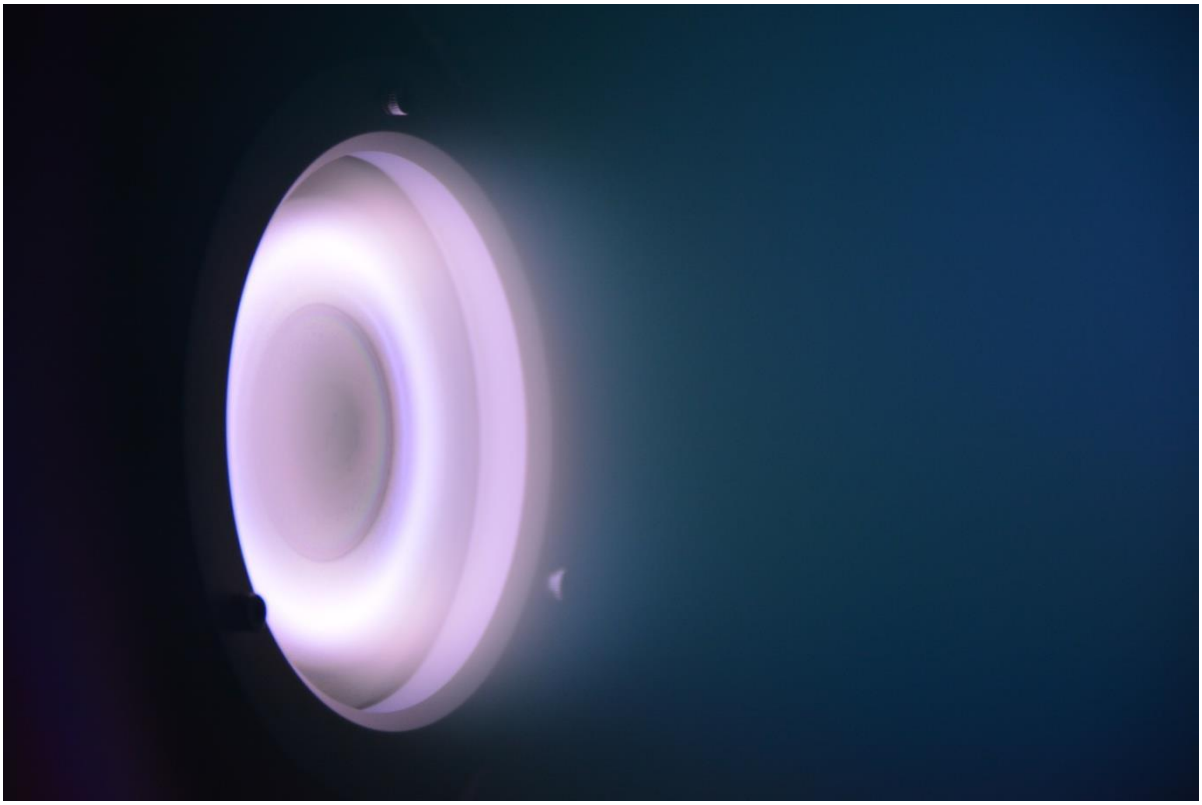

Figure 2-10 Magnetron discharge with plasma ring caused by magnetic field.

Magnetrons can be powered by a variety of methods. It can be chosen among radio frequency (RF), direct current (DC), pulsed DC and, recently, high-power impulse magnetron sputtering [4].

2.4.2 HiPIMS

The high-power impulse magnetron sputtering (HiPIMS) is a modern method of plasma based sputtering technology. In principle, in HiPIMS, a high power is applied to the target of the magnetron during unipolar pulses at low repetition frequency and low duty cycle while the peak power is about two orders of magnitude higher than the average power.

In conventional dc magnetron sputtering the sputtered vapor consists primarily of neutral particles which is the major disadvantage compared to HiPIMS [8].

HiPIMS has been successfully involved into various industrial applications and so it is an established technique for ionized physical vapor deposition processes [8].

HiPIMS uses a large energy pulses supplied to the cathode over a very short period, typically ~100 μs [4]. This requires a very different type of power supply, which is based on a large bank of capacitors, as shown in figure 2-11. Peak powers up to several kW/pulse with pulse widths between 100 and 150 μs must be generated by the power supply with average powers ~ 100 W – 1 kW and frequencies up to 500 Hz, having arc suppression [4]. This process takes advantage of enhanced ionization resulting from the high-energy pulse. Peak power densities applied to the target are close of 1–3 kW/cm^2, compared to traditional magnetron sputtering with power densities ~1–10 W/cm^2 [4].

The HiPIMS discharge operates with a cathode voltage in the range of 500–2000 V, current densities of up to 3–4 A/cm^2, peak power densities in the range of 0.5–10 kW/cm^2, repetition frequency in the range of 50–5000 Hz, and duty cycle in the range of 0.5%–5% [8]. Although the peak power is 2–3 orders of magnitude larger than commonly used in a conventional DC discharge, the average power is the same [8].

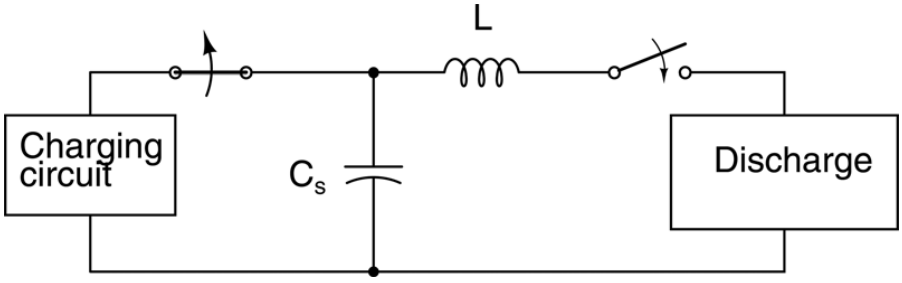

Figure 2-11 The very basic schematic of HiPIMS circuit. C_S - a large bank of capacitors. Opening and closing of switch is usually controlled by generator of periodic signal. [8]

One of the most important process parameters is the plasma density, since it affects both the deposition rate as well as the ionization fraction of the sputtered material flux. The plasma density increases with increased power density supplied to the target. But increased power density leads to overheating and eventually melting of the sputtering target [8]. HiPIMS can reach increased power density without risking of target damage, because the high power is delivered to the system only during short pulses and a long pause exists between the pulses so the cooling system remove heat from the target sufficiently.

For many applications, a high degree of ionization of the sputtered vapor is desired as the ion flux to the substrate is known to have a significant influence on the overall quality of the resulting film. Ionized flux of the sputtered vapor therefore introduces an additional control parameter into the deposition process. Increased ionization of the sputtered vapor gives improvement of the film quality, such as density, higher hardness, improved adhesion, improved surface roughness, control of the reactivity and guiding of the deposition material to the desired areas of the biased substrate. Also, the deposition temperature can be lower while maintaining the film quality. Furthermore, due to the pulsed nature of the deposition flux the instant deposition rates are very high, giving a high supersaturation of adatoms on the growth surface. This leads to changed growth conditions with flat films and dense microstructures as a result [8].

HiPIMS results in high ionization fraction of the sputtered material, and a high plasma density, which brings new ways of control of the film preparation by adjusting the energy and the deposition species direction [8].

The parameter range is much wider in the pulsed system compared to conventional dc and radio frequency (RF) operation and the pulsing of the discharge allows for a much greater flexibility due to additional control parameters such as pulse width, duty cycle, and pulse frequency.

2.5 Applications of deposited processes

Some of the most utilized applications of thin film deposition processes include:	
• Single and multilayer films and coatings • Nanolayered materials • Optical films for transmission and reflection • Decorative films • Decorative and wear-resistant (decorative/functional) coatings • Permeation barriers for moisture and gases • Corrosion-resistant films • Electrically insulating layers for microelectronics • Coating of engine turbine blades • Coating of high strength steels to avoid hydrogen embrittlement	• Diffusion barrier layers for semiconductor metallization • Magnetic films for recording media • Transparent electrical conductors and antistatic coatings • Wear and erosion-resistant (hard) coatings (tool coatings) • Dry film lubricants • Composite and phase-dispersed films and coatings • Nanocomposite materials • Thin-walled freestanding structures and foils

Some materials deposited by PVD processes are as follows.

Elements:	• Gold – electrical conductor, anticorrosion surface, surface replication, bondable surface, infrared (IR) reflectance • Silver – electrical conductor, heat reflector, optical mirrors, low shear solid film lubricant • Aluminium – electrical conductor, optical reflectance, corrosion resistance, permeation barrier • Copper – electrical conductor, solderability • Cadmium – corrosion resistance (being phased out) • Zinc – corrosion resistance • Titanium – “glue layer” to oxides • Chromium – “glue layer” to oxides, corrosion resistance, hard coating • Palladium – galvanic corrosion layer between Ti and Au • Molybdenum – “glue layer” to oxides • Tantalum – corrosion and erosion resistance • Beryllium – freestanding X-ray windows • Carbon (DLC) – hard coat, chemically resistant, low friction • Nickel – “glue layer” to metals, basecoat on brass • Silicon – semiconductor devices • Selenium – photosensitive material

Mixtures (above solubility limits):	• Silicon + dopants – semiconductor devices • Nanophase composites – hard coatings
Glasses:	• Amorphous silicon (a–Si) – semiconductor, photovoltaic • Phosphorus + silicon oxides (PSGs) – encapsulant
Alloys:	• Zinc + aluminium – corrosion protection • Aluminium + copper + silicon – semiconductor metallization • Indium + tin/oxide – transparent electrical conductor, IR reflection • Nickel + chromium – "glue layer" to oxides, electrical resistance • Tungsten + titanium – semiconductor metallization, diffusion barrier
Compounds:	• Titanium nitride – diffusion barrier coating, tool coating, decorative coating • Titanium/Carbon nitride – tool coating, decorative coating • Titanium/Aluminium nitride – wear coating • Chromium nitride – hard coating, low friction • Aluminium oxide – permeation barrier, diffusion barrier • Titanium oxide – high index optical coating • Silicon dioxide – low index optical coating • Magnesium fluoride – low index optical coating • Molybdenum disulphide – solid film lubricant • Molybdenum diselenide – solid film lubricant (electrical conductor) • Tantalum oxide – high index optical coating • Zinc sulphide – high index optical coating
Layered systems:	• Ti/Au, Ti/Pd/Cu/Au, Ti/Ag, Ti/Pd/Ag – electrical conductor electrodes on oxides • Cr/Au, Cr/Pd/Au – oxide metallization • Mo/Au – oxide metallization • TiN/Al – silicon metallization • Ni/Cr – basecoat on brass • Nanolayered composites – hard/wear coatings • ZnO_x: Ag: Zn (thin): ZnO_x: TiO_x – low-e (low emission) glass coating • SnO_x: Ag: NiCr (thin): SnO_x – low-e glass coating on glass

The previous list shows the vast versatility of physical vapor deposition processes [1].

2.6 Transparent electrically conductive oxides

Indium tin doped oxide (ITO) is a transparent conductive oxide (TCO) film which has a large application benefits. The application potential of TCO films is predetermined by the film resistivity (which is typically wanted to be low) and transparency (which is expected to be high).

The main aim of this thesis was production of thin films that could be conductive as well as transparent at the same time. The films must be optimized for the purposes of development of new type of biosensors. The biosensors are optical fibres covered by the functional conductive and transparent film which should be able to perform combination of simultaneous optical and electrochemical measurements. For this purpose indium tin oxide (ITO) was selected as a functional film.

Indium tin oxide is a ternary composition of indium, tin and oxygen with variable stoichiometry. Depending on the oxygen content, it can either be described as a ceramic or alloy. Indium tin oxide is typically encountered as an oxygen-saturated composition. Oxygen-saturated compositions are so common, that unsaturated compositions are termed *oxygen-deficient ITO*. Indium tin oxide (ITO) is an optoelectronic material that is applied widely in both research and industry [6].

Indium Oxide/Tin Oxide (In_2O_3/SnO_2 90/10 WT%) is among one of the most heavily utilized compounds in the thin film industry mainly for two of its significant properties:

- optical transparency
- electrical conductivity

Specifically, the 90/10 WT% composition has a melting point of approximately 1,800°C and a density of 7.14 g/cm^3 [6]. The colour of various ITO compounds range from pale yellow to dark green or dark grey [6].

Optical transparency

ITO is a n-type semiconductor with a great bandgap of around 4 eV, which is the reason why it is mostly transparent in the visible part of the light spectrum and its extinction coefficient, *k*, is zero in this wavelength range. In the ultraviolet (UV) spectral range and in the near infrared (NIR) and infrared (IR) spectral range, ITO is opaque, so that *k* is non-zero in the UV, NIR and IR. UV opacity is due to band-to-band absorption (an electron in the valence band can be excited to the conduction band due to the UV photon energy). NIR and IR opacity is caused by absorption of free carrier (an electron on a lower energetic state within the conduction band can excite to higher energetic state within the conduction band by an infrared photon). In these wavelength ranges *k* is non-zero. For NIR and IR wavelength range reaches its maximum value in the IR regime, where it shows similar behaviour of *k* like for metals [9].

Electrical conductivity

The high conductivity of ITO is related to the presence of shallow donor or impurity states located close to the host (In_2O_3) conduction band, and produced via chemical doping of Sn^{4+} for In^{3+} or by the presence of oxygen vacancy impurity states. Each oxygen vacancy acts as a doubly charged electron donor if present in the lattice. Therefore, ITO films are usually grown in chemically reducing environments, which encourage oxygen vacancy formation to enhance their electrical properties. The proximity of any such electronic states to the host conduction band necessitates their classification as shallow donor or impurity states, whereby the excess or donor electron undergoes thermal ionization at room temperature into the host conduction band [10].

As with all transparent conducting films the goal is usually to produce film with high transparency and high conductivity. Unfortunately, these two features are contradictory. With the increased concentration of the free charge carriers the conductivity of the material is increased, but the transparency is decreased, so a compromise between conductivity and transparency must be usually made.

ITO has attractive properties including high level of transmittance in the visible region as well as electrical conductivity that is unique. This is mainly due to ITO's highly degenerate behaviour as an n-type semiconductor with a large band gap of around 3.5 to 4.3 eV [11].

ITO can be used for many applications, such as smart windows, polymer-based electronics, thin film photovoltaic, anti-reflective coatings, architectural windows and electroluminescence, where the thin films are used as conductive, transparent electrodes.

Figure 2-12 Aircraft windshields. The interference is caused by non-uniform ITO film thickness across an Airbus cockpit window serving as a defrosting coating [Downloaded from internet].

ITO is often used to make transparent conductive coatings for displays such as liquid crystal displays (LCDs), flat panel displays, plasma displays, touch panels, and electronic ink applications. Thin films of ITO are also used in organic light-emitting diodes, solar cells, antistatic coatings and EMI shielding [11].

ITO films can be deposited on glass window to serve as defrosting layer, for example, for aircraft windshields as shown in figure 2-12. The heat is generated by electrical current flowing through the film.

Thin films of ITO are created for the development of sensors, as well as, a glass coating for the automotive industry.

Thin films of indium tin oxide are most commonly deposited on surfaces by physical vapor deposition. Often electron beam evaporation, or another sputter deposition techniques are used.
In this work, ITO layers were prepared by magnetron sputter deposition in a plasma environment.

3 Diagnostic methods used in this work

This chapter brings introduction into several diagnostical methods used in this work concerning plasma diagnostics, studying deposition process itself, and surface diagnostics, used for analysis of deposited layers.

3.1 Plasma diagnostics

The following methods were used for the plasma diagnostics:

- Optical emission spectroscopy
- Langmuir probe diagnostics

3.1.1 Optical emission spectroscopy

Optical diagnostic is contactless diagnosis which uses plasma radiation in the visible spectrum or in the infrared and ultraviolet. Radiation of atoms and ions (or molecules) in the transition process from an excited state to a lower energy state is used. If the line spectrum is predominant, then it is possible to determine the relative concentrations of the short-lived excited states (<100 ns) from a relative intensity of radiation. In addition to the states with a short life span there are also excited particles with long life span (> 1 μs) in the plasma, of which the most important is the role of metastable states. Metastable states are of great importance for the Penning ionization.

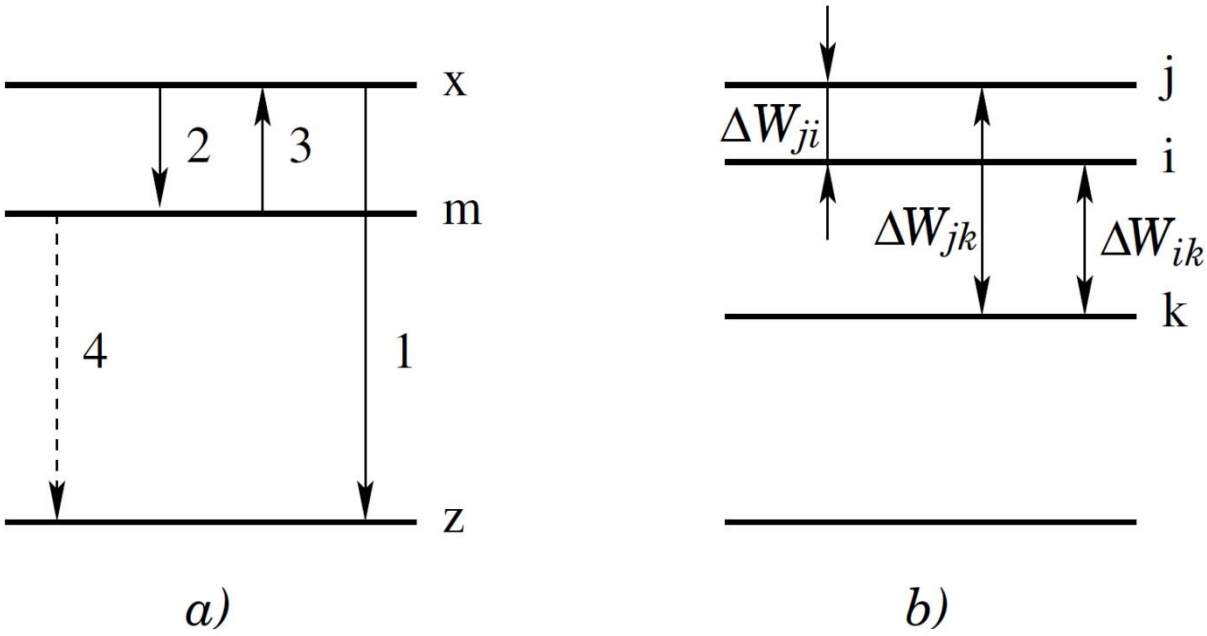

Figure 3-1 Energetic levels of atom: a) transitions between states: z – ground state, x – the short-lived excited states, m – metastable state; b) energetic differences between states [3].

In technical practice, it is sometimes a problem that the radiation emitted during the transition to lower energy states are subject to rapid absorption of gas; such radiation is called the resonance radiation. This radiation moreover sometimes lies outside the visible light region. For these two reasons are selected such transitions between energy levels, which emit radiation without these problematic properties.

Plasma spectroscopy can be used also to determine the chemical composition of the particles in the plasma by the occurrence of the characteristic spectral lines. From the intensities of spectral lines and their width it is also possible to determine the temperature and concentration of plasma electrons.

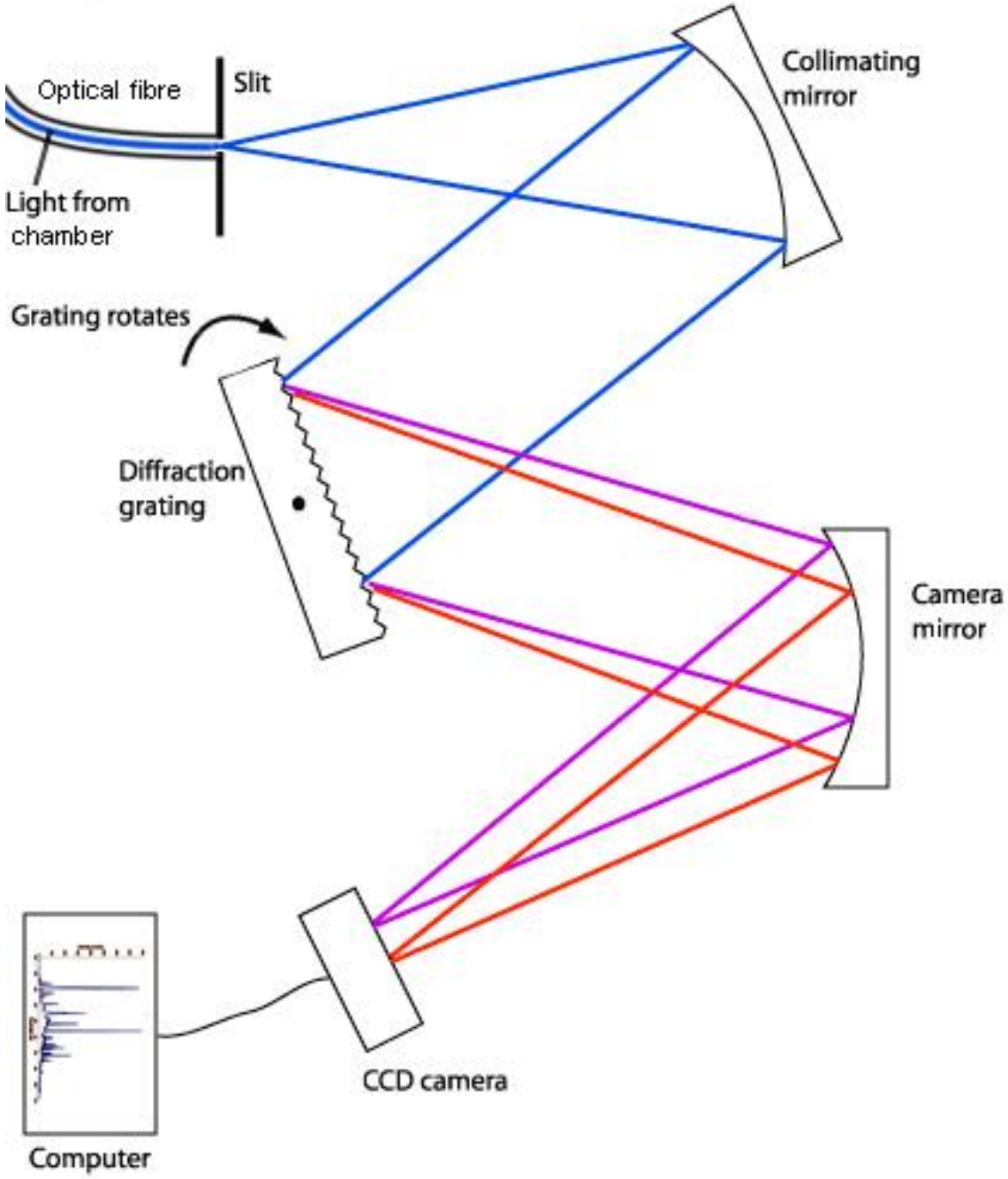

Figure 3-2 Schematics of the spectrograph. The light from the chamber is delivered through an optical fibre into the spectrograph, where it is diffracted by an adjustable diffraction grating. Diffracted light is afterward captured by a CCD chip and the spectrum lines are analysed by a computer [downloaded from internet and changed].

For plasma discharge performed in the frame of this thesis, spectrograph ANDOR SR-500i-B1-R and equipped by ANDOR iSTAR iCCD 340 camera was used.

3.1.2 Langmuir probe

Electrostatic probe, also called Langmuir probe, is a metal electrode inserted into the plasma. It is most often made of noble metal wire (platinum, molybdenum or tungsten) because of their sufficiently high melting point and resistance against charged particles bombardment. The electrode is placed in the tube of the insulator from which the probe tip protrudes into the plasma. The probe may be of various shapes, as shown in figure 3-3. In practice, the most used is the cylinder probe.

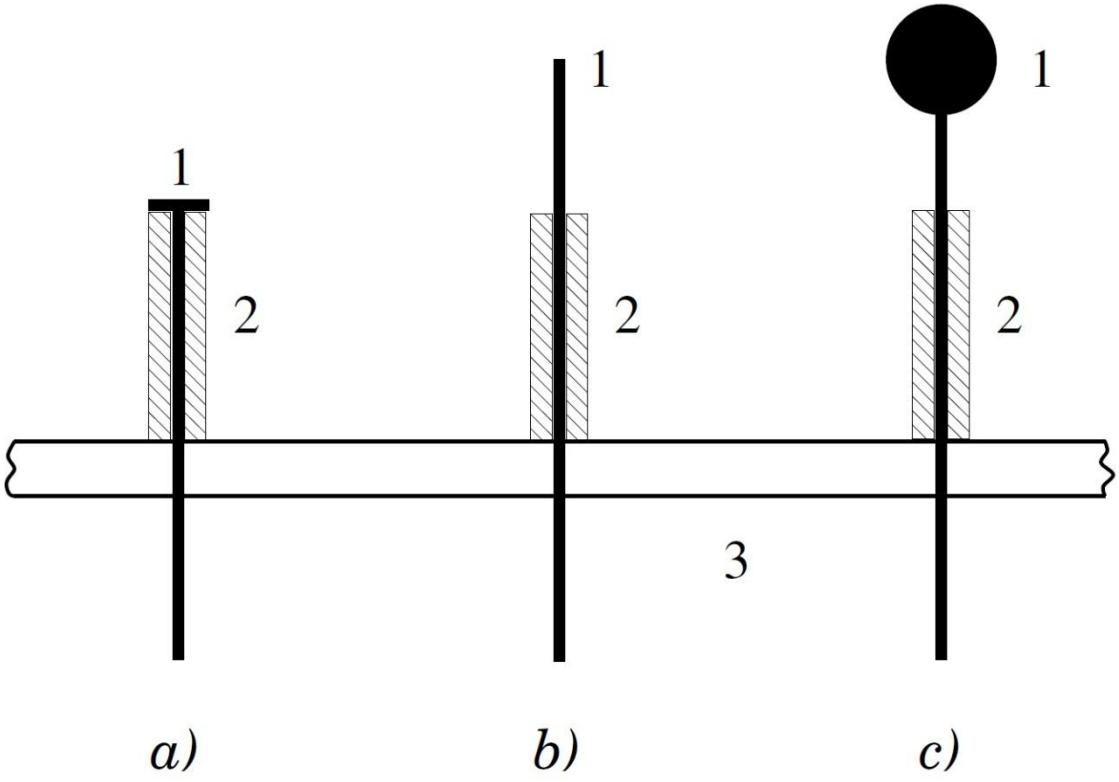

Figure 3-3 Construction of the electrostatic probe: a) planar probe; b) cylinder probe; c) spherical probe; 1 – probe; 2 – insulator; 3 – wall [3].

This method is based on measurement of V-A characteristics obtained by application of voltage to the probe and measurement of the current flowing through the probe. The electrode potential φ_p can be changed by its connection in the electrical circuit. To create a closed circuit, it is required to have the reference electrode in plasma. If at least one electrode of plasma discharge (anode or cathode) is used as the reference electrode the

arrangement is called single probe method. In the case of electrodeless discharge, such as microwave discharges, second probe is inserted into the plasma near the first and it serves as a reference electrode.

Around the probe with the potential φ_p located in the plasma, a layer of the space charge is formed, which is proportional to the voltage of the probe and the plasma potential. This field attracts one type of the charged particles, repels the second.

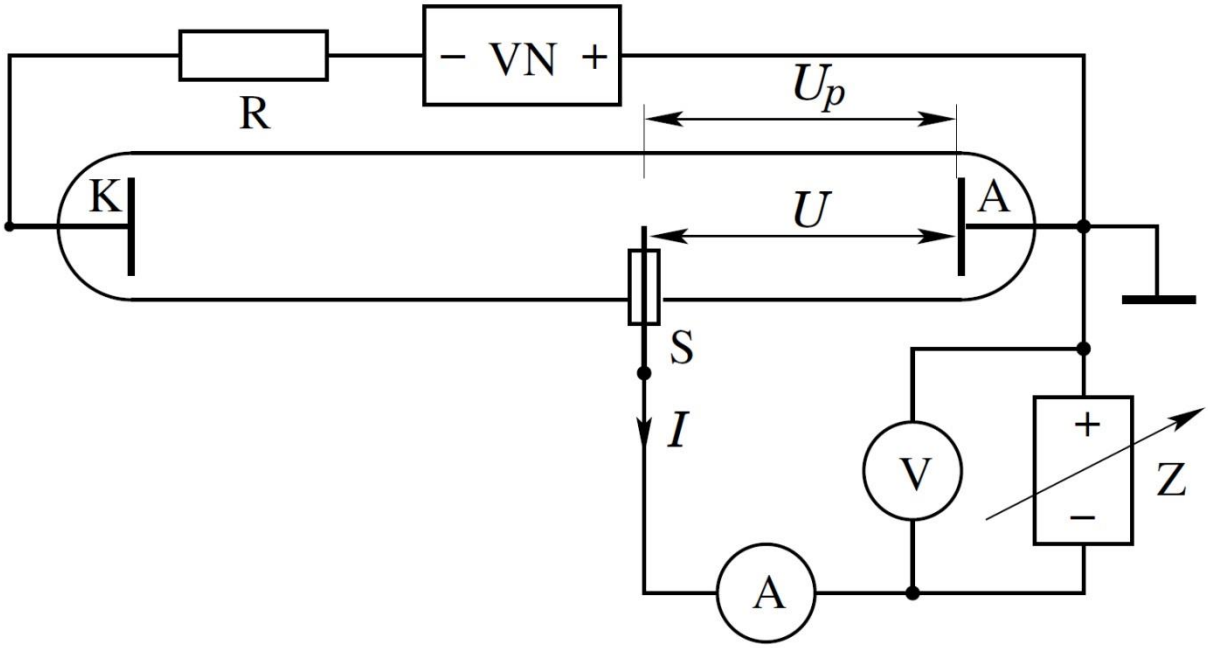

Figure 3-4 Diagram of the possible connection of the probe for diagnostics of the glow discharge (anode A serves as the reference electrode): S – probe; VN – High voltage source for powering plasma discharge; R – resistor in series for stabilization of the discharge current; Z – adjustable source of voltage (to set potential of the probe); V and A – voltmeter and amperemeter; I – probe current, U - voltage between probe and anode; Up – intact plasma potential at the site of the probe to the anode (plasma potential) [3].

The result represents a volt-ampere characteristic of the probe, which expresses the dependence of the current passing through the probe to a connected voltage. The typical shape of the V-A characteristics is shown in figure 3-5.

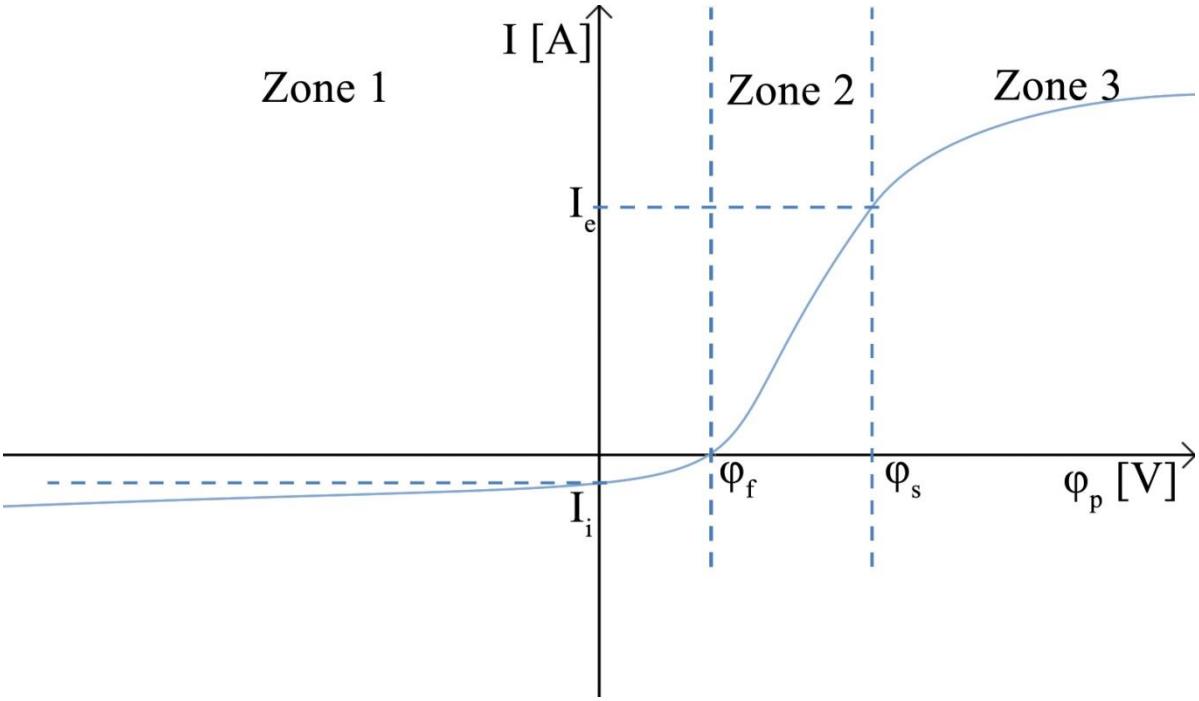

Figure 3-5 Typical shape of V-A characteristic of glow discharge: φ_p – probe potential; φ_f – floating potential; φ_s– plasma potential; I – current passing through the probe; I_e – border of electron saturation current area; I_i – border of ion saturation current area;

There are two important points in V-A characteristics:

Floating potential, φ_f – the probe current is 0.

Plasma potential, φ_s – the plasma potential is at the inflection point of V-A characteristics

The figure 3-5 shows that the V-A curve can be divided into three areas by these two points:

- Zone 1

  — $\varphi_p < \varphi_f$ — Negative potential of the probe causes the attraction of ions and repulsion of electrons, ion current to probe prevails over the current of electrons $I < 0$.

  — $\varphi_p = \varphi_f$ — The potential of the probe cause the current of ions and electrons to be equal; $I = 0$.

- Zone 2

  — $\varphi_f < \varphi_p < \varphi_s$ — Electron current prevails; $I > 0$.

  — $\varphi_p = \varphi_s$ — Barrier for electrons completely vanishes, the total current to the probe is given by the difference of non-reduced currents of electrons and ions that are a consequence of their thermal motion. The probe with the plasma potential do not interfere quasi-neutrality of plasma at the insertion site so a space charge region does not form near the probe.

- Zone 3

  — $\varphi_p > \varphi_s$ — The area of electron saturation current. The ion current to the probe is reduced due to the potential barriers that ions must overcome. The probe disrupts the plasma quasi-neutrality, it collects electrons around it.

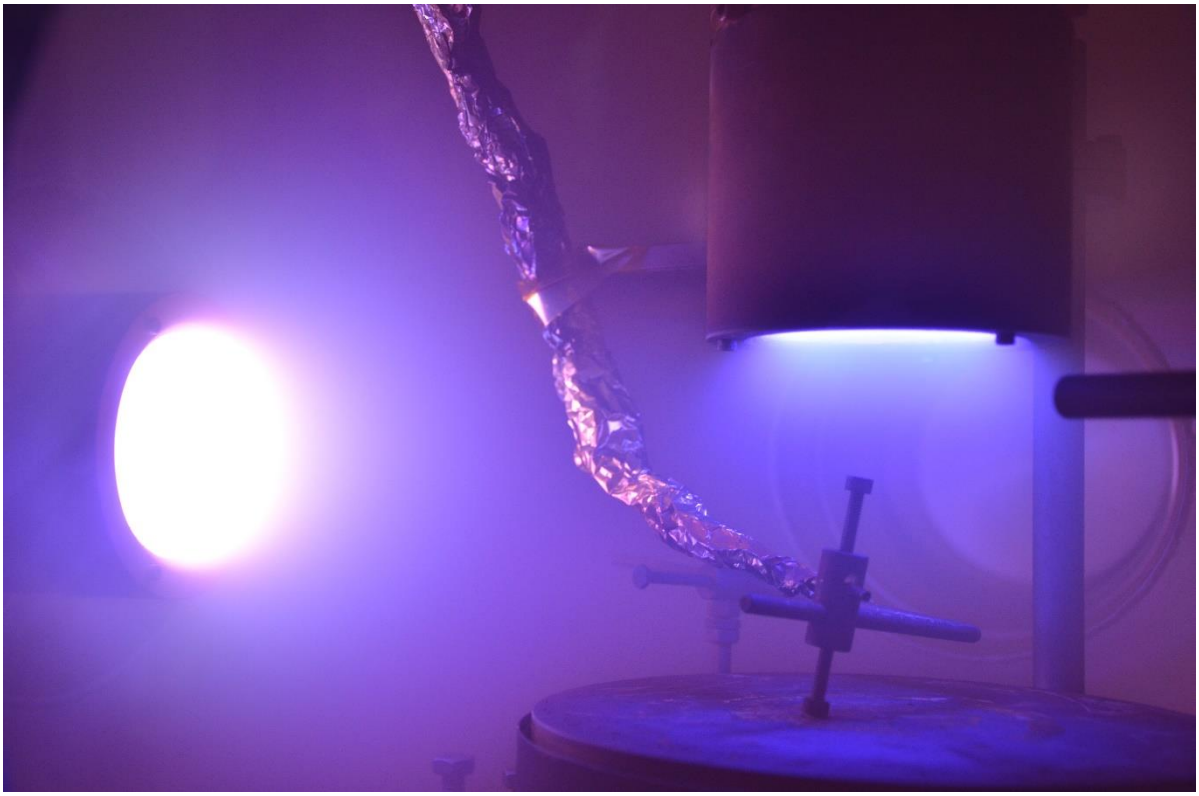

Figure 3-6 View into the chamber during plasma diagnostic by Langmuir probe positioned above substrate holder.

Using Langmuir probe, it is possible to determine the electron temperature, electron concentration, energy distribution, plasma density, plasma potential and the floating potential [12].

The electron energy probability function (EEPF) can be estimated in terms of the measured value of $\frac{d^2 i_e}{dV^2}$ by the equation:

$$F(\varepsilon) = \varepsilon^{-\frac{1}{2}} f(\varepsilon) = \frac{4}{e^3 A_p} \sqrt{\frac{m_e}{2}} \frac{d^2 i_e}{dV^2} \qquad \text{Eq. 8}$$

Where $f(\varepsilon)$ is the electron energy distribution function (EEDF), A_p denotes the probe surface, e is elementary charge, m_e is electron mass, i_e is electron probe current, and V is the applied voltage [12].

Electron temperature T_e is estimated from the inverse slope of the logarithmic electron probe current i_e with respect to the probe voltage V

$$T_e = \left[\frac{d \ln i_e(V)}{dV}\right]^{-1} \qquad \text{Eq. 9}$$

The mean electron energy E_m can be determined from the integrated distribution function:

$$E_m = \frac{1}{n_e} \int_0^\infty \varepsilon\, f(\varepsilon)\, d\varepsilon \qquad \text{Eq. 10}$$

The electron density is determined by the equation

$$n_e = \int_0^\infty f(\varepsilon)\, d\varepsilon \qquad \text{Eq. 11 [12]}$$

The system for the Langmuir probe measurement in this thesis was from company Impedans, model: ALP 150.

3.2 Surface diagnostics

The following methods were used for the surface diagnostics:

- Four-point probe method
- Atomic force microscopy
- Optical absorption spectroscopy
- X-ray diffractometry

3.2.1 Four-point probe method

Four-point probe was a method used in this work for a measurements of thin films resistivity ϱ. Four electrodes are applied to the layer in a line, as shown on the figure 3-7**.** The outer electrodes are connected to a source of electrical current. The inner electrodes are connected to a voltmeter to measure the voltage induced by the current flowing through the sample.

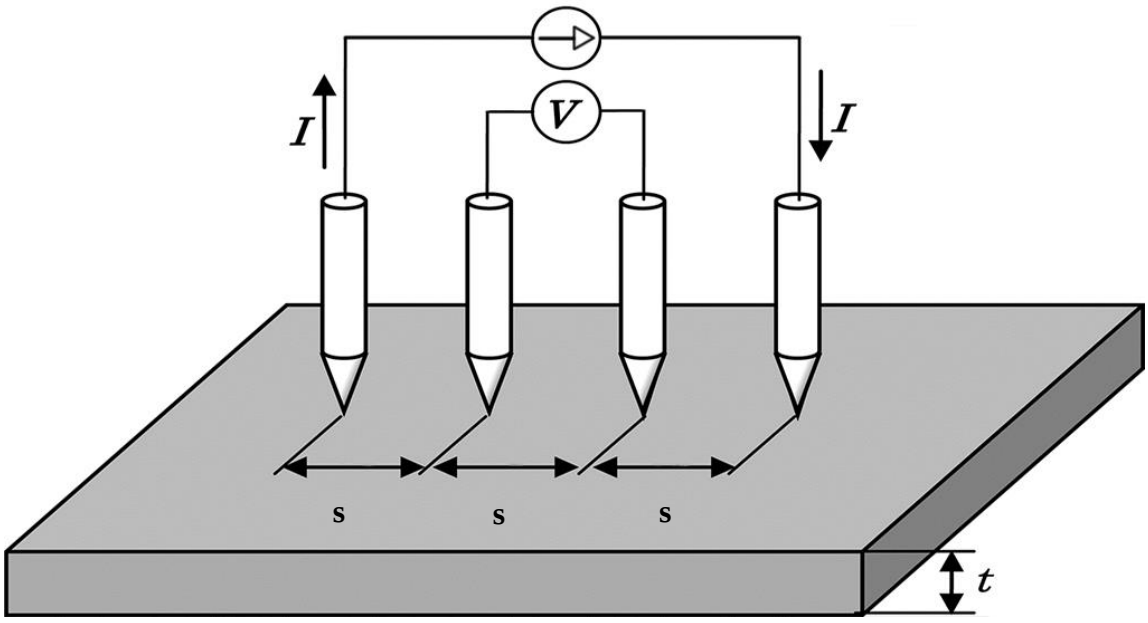

Figure 3-7 Schematics of the four-point probe measurements. I is electrical current, s is electrode spacing and t is the thickness of the film. Modified from [13]

The film resistivity is given by:

$$\varrho = \frac{V}{I} t \frac{\pi}{ln\,2} f\left(\frac{t}{s}\right) \qquad Eq.\ 12$$

Where I is the applied electrical current, V is the measured voltage, t is the thickness of the film, s is electrode spacing and f (t/s) is the shape correction coefficient, which becomes 1 for $s \gg t$ [13].

3.2.2 Atomic Force Microscopy

Atomic Force Microscopy (AFM) is scanning probe technique that permits imaging of surfaces down to the atomic level. But unlike scanning tunnelling microscope (STM), in which the tunnelling current between an electrode and the sample is used to produce images, AFM monitors the force between a sharp tip and the sample and utilizes this force to produce images. In many other respects, it is similar to an STM: there is a piezoelectric actuator to precisely control the sensor above the surface and to raster the tip across the sample, also a control system to provide feedback to the piezoelectric actuators and display the images is included, and an isolation system to damp vibrations is involved in the measurement. A schematic of the instrument is depicted in figure 3-8. In this case, the probe is a microfabricated, cantilevered, force sensor that deflects as a result of the sample-induced forces placed on the sharp tip that is positioned on or above the sample surface. The cantilever deflects upward in the case of a repulsive force, or downward in the case of an attractive force. The extent of deflection is proportional to the force applied to the sensor and is generally described by Hooke's law.

$$F = kx$$

where F is the force exerted on the cantilever, k is the spring constant of the cantilever, and x is the distance of deflection. The deflection can be measured using an optical lever, in which a laser diode is focused on the end of the cantilever, which is typically angled downward from horizontal at $\sim 10^{\circ}$. The reflective coating on the back side of the cantilever permits reflection of the laser light to a position-sensitive photodiode detector located some distance away from the cantilever. A deflecting cantilever changes the position of the laser spot on the photodiode, which is monitored by the control system. In the case of an AFM, this deflection, usually associated with topography, is utilized to generate an image of the sample surface. One specific advantage AFM has over STM is its ability to image non-conducting samples [4].

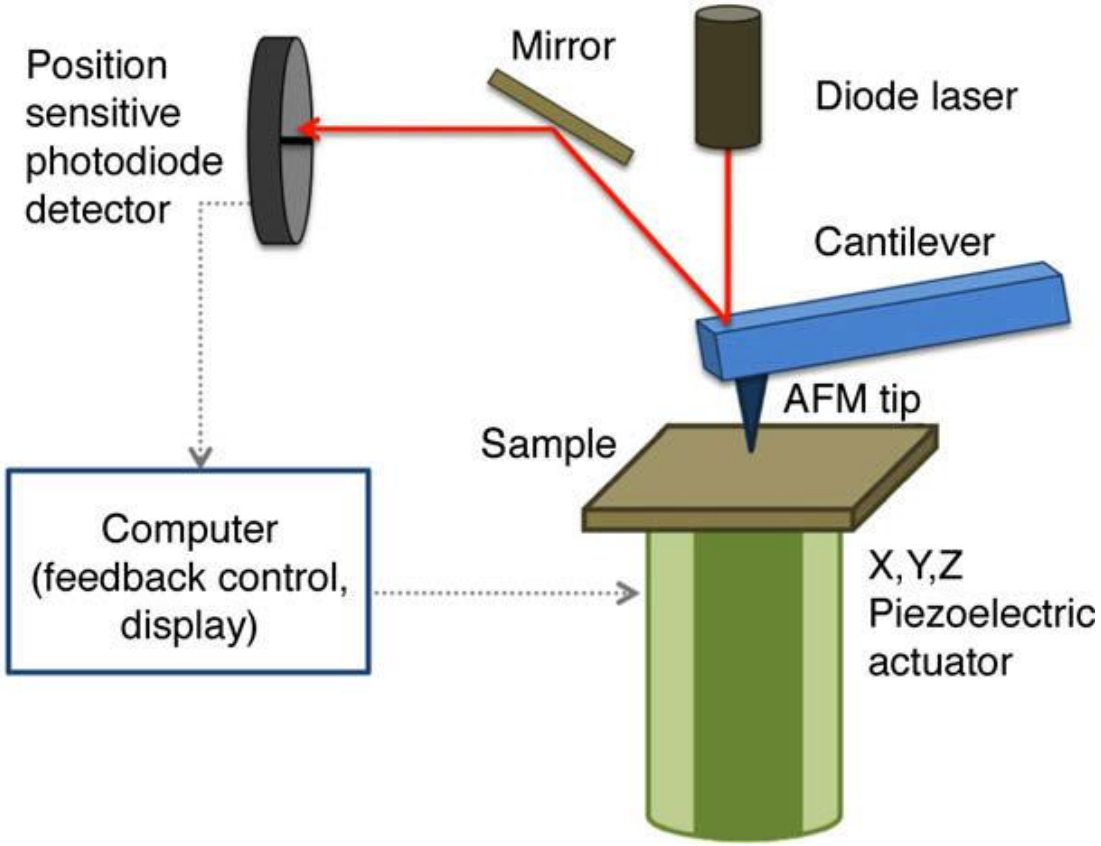

Figure 3-8 Schematic of the AFM [4]

Atomic force microscopy images in this thesis were obtained in air on a Veeco Metrology system (Model No. 920-006-101) operating in the tapping mode when cantilever is oscillating and not in continuous contact with the surface to reduce damage of the sample by the tip.

3.2.3 Optical absorption spectroscopy

Spectrophotometry is the quantitative measurement of the transmission properties of a material as a function of wavelength. Spectrophotometry usually deals with visible light, near-ultraviolet, and near-infrared, but does not include time-resolved spectroscopic techniques.

Spectrophotometers can measure a light beam's intensity as a function of its wavelength. Important features of spectrophotometers are spectral bandwidth (the colours range it can transmit through the test sample), the percentage of sample-transmission and the logarithmic range of sample-absorption.

Spectrophotometers can usually be divided in two major classes: single beam and double beam. Single-beam devices measure the relative light intensity of the beam before and after a test sample is inserted or changed. A double beam devices compare the light intensity between two light paths, one path leads through a reference sample and the other through the test sample. On one hand, measurements from double-beam instruments are usually more stable and easier, on the other hand, single-beam instruments can have a larger dynamic range and are optically simpler and more compact.

When making absorbance measurements, the spectrophotometer quantitatively compares the light that passes through the reference sample and the test sample, then compares the intensities of the two signals and computes the percentage of absorbance of the sample compared to the reference standard.

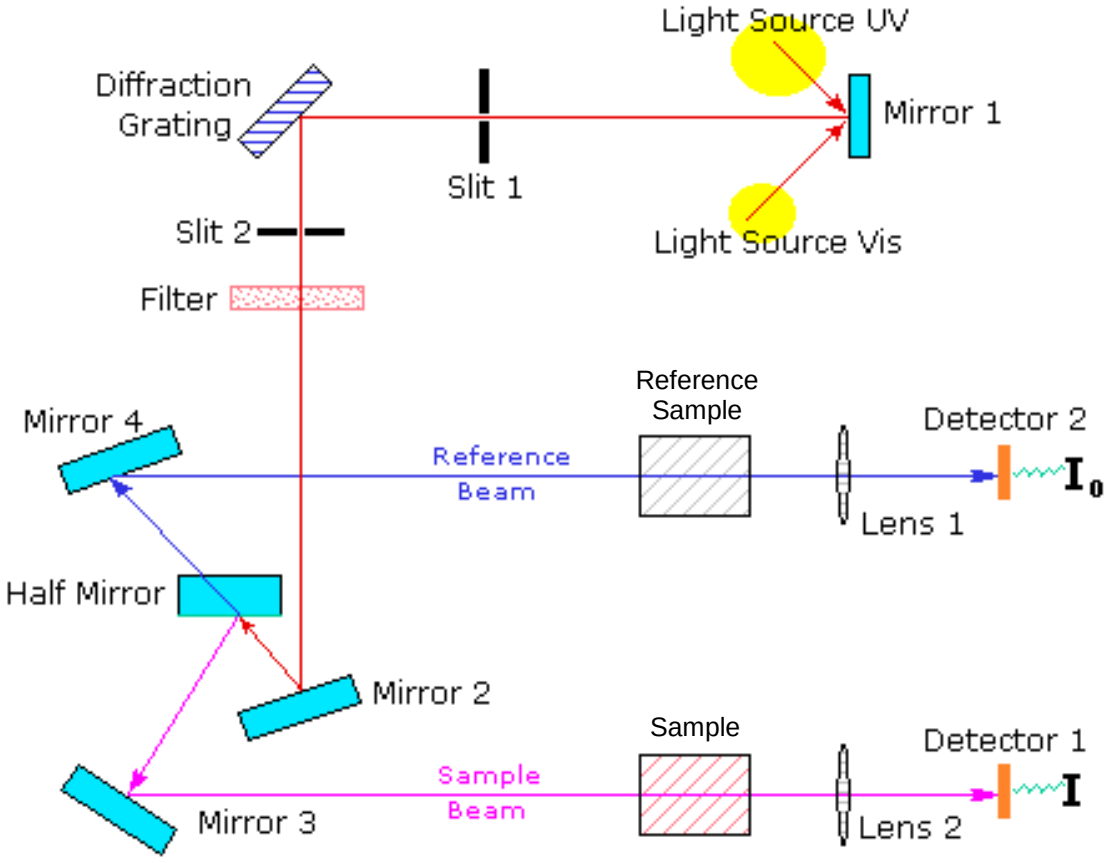

Figure 3-9 Schematic of the double beam spectrophotometer shows a path of the light beam from a source to a diffraction grating where the wavelength is chosen. The selected wavelength travels through a half mirror where the beam is split into two beams, one for the sample, the second for the reference, each going to a detector behind the sample or reference sample. Downloaded from [14].

SHIMADZU spectrophhotometer UV-1800 was used for absorption measurements of deposited films. As a reference sample, microscopic glass was used.

3.2.4 X-ray diffractometry

X-ray diffractometry (XRD) is one of the most powerful non-destructive bulk techniques for analysing a wide range of materials from research and development to production and engineering environments. Because of the advancements in instrument engineering, technology, and computational aspects, XRD methods are being applied for a wide range of materials, enabling answers to many different types of diffraction challenges. Many of these methods apply to characterization of thin films. Applications include phase analysis, determination of crystalline structure and epitaxial orientation, measurement of thickness and interfacial roughness, determination of texture and residual stress in films, studies of nanomaterial development and measurements of their reactivity, and polymorph screening [4].

In principle, XRD is based on a measurement of an intensity and angle of X-rays diffracted on a crystalline structure of the sample. Crystals are regular arrays of atoms, and X-rays are waves of electromagnetic radiation. Atoms scatter X-ray waves, primarily through the electrons in atomic orbitals. The X-ray striking an electron produces secondary spherical waves spreading from the electron. This effect is known as elastic scattering, and the electrons are known as the scatterers. A regular array of scatterers produces a regular array of spherical waves. In most directions, these waves cancel one another through destructive interference, but they interfere constructively in a few specific directions, determined by Bragg's law:

$$2d \cdot \sin\Theta = n\lambda \qquad \text{Eq. 13}$$

Where d is the spacing between diffracting planes, Θ is the incident angle, n is any integer, and λ is the wavelength of the beam.

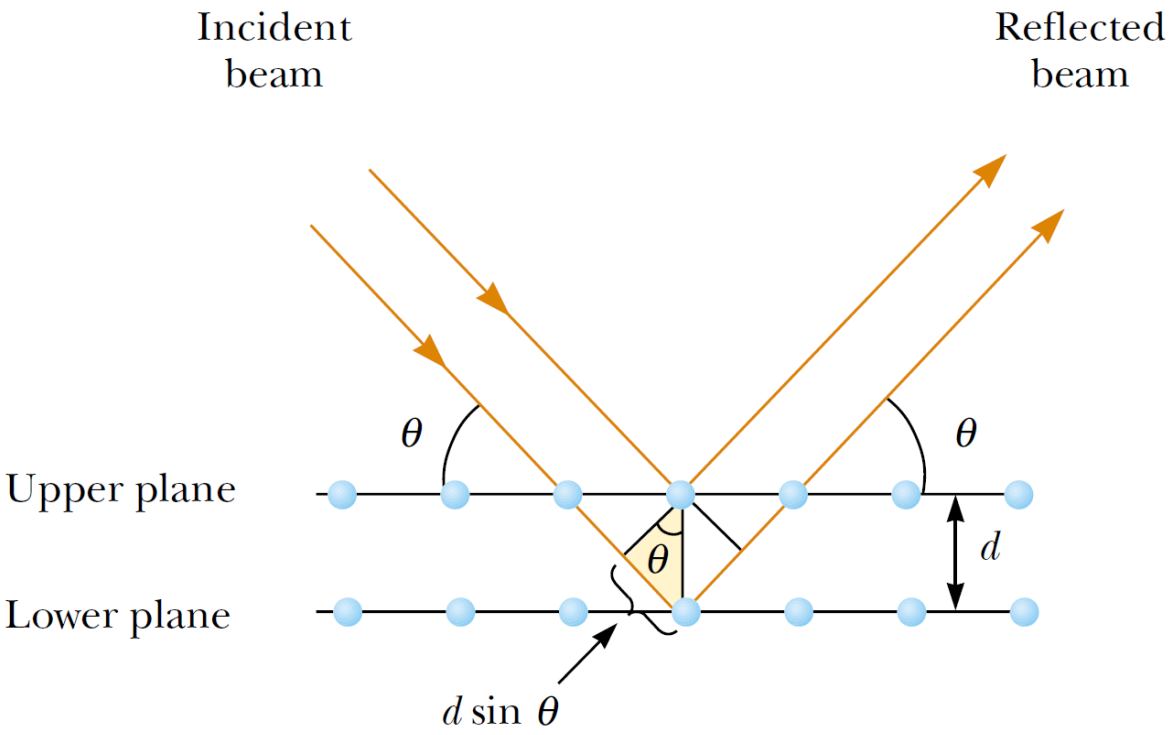

Figure 3-10 A two-dimensional description of the reflection of an x-ray beam from two parallel crystalline planes separated by a distance d. The beam reflected from the lower plane travels farther than the one reflected from the upper plane by a distance 2d sin Θ [15].

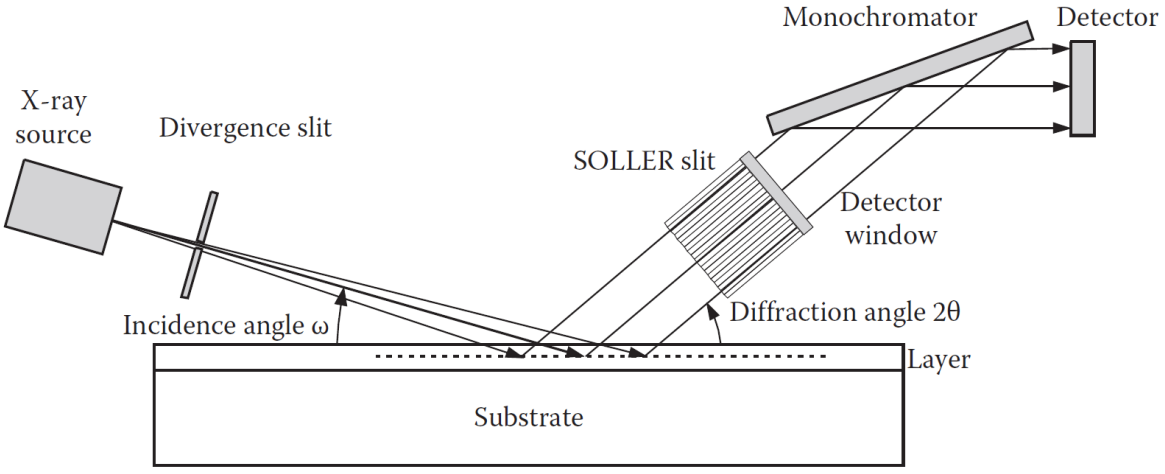

Figure 3-11 Schematics of XRD for thin layer [16]

4 Experimental facility

All deposition processes were performed in the vacuum chamber.

The chamber has a shape of a cylinder with the radius 25 cm and height 52 cm.

It has 10 feedthroughs for connection of devices necessary for deposition experiments and plasma diagnostics.

High vacuum in the chamber is achieved by the two pumps set in series:

- Rotary pump (EDWARDS XDS35i), serving as a secondary pump, to achieve low pressure up to 5 Pa

- Turbo molecular pump (PFEIFFER VACUUM TC400), serving as a primary pump, reaching pressure up to 10^{-4} Pa.

The pressure in the chamber was measured by Compact cold cathode gauge (PFEIFFER VACUUM IKR 251) and Compact pirani capacitance gauge (PFEIFFER VACUUM PCR 260).

Insertion of the working gasses is achieved by a MKS Instruments mass flow controllers.

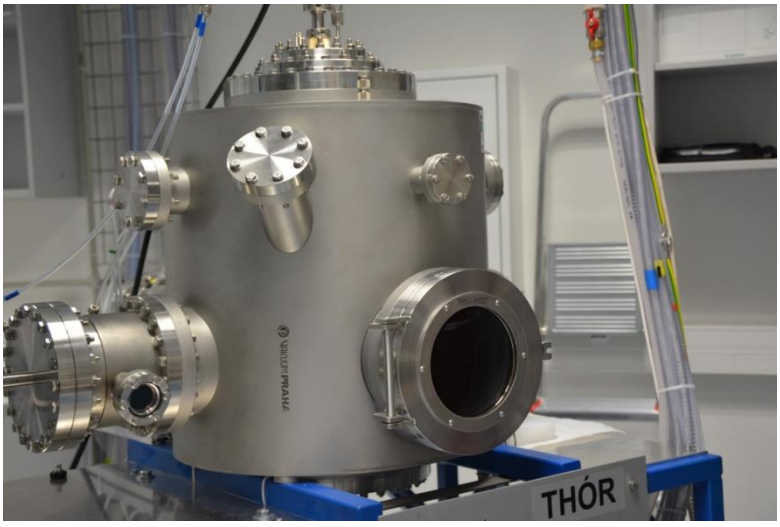

Figure 4-1 THOR – vacuum chamber used for the deposition process.

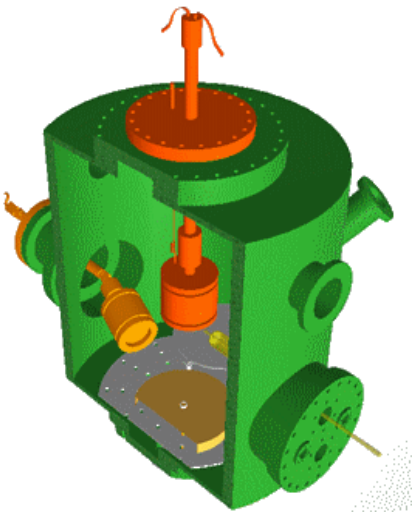

Figure 4-2 3D scheme of THOR showing orientation of the two magnetrons (yellow and orange) used for the deposition of ITO.

Chamber was equipped with two 3“magnetrons in positions with perpendicular axis as shown on figure 4-2. Both had inserted ITO targets. The bottom magnetron was supplied by HiPIMS unit. The DC power source for supplying HiPIMS was Heinzinger PNC 1500-1200. The upper magnetron was supplied by RF source (COMET Cito 1310-ACNA-P37A-FF).

Voltage and current was measured and displayed by four-channel digital oscilloscope Tektronix MDO3034.

5 Experimental part

As previously mentioned, the goal of this work was a preparation the ITO thin films with the high conductivity and the high transparency using magnetron sputtering. Electrical as well as optical properties of ITO films are strongly influenced by the film crystallography. It is well known that film properties are strongly influenced by deposition process parameters. Hence, optimizing the deposition conditions, it is possible to tune the film properties. This thesis aims to study the deposition process of ITO from the point of view of plasma diagnostics as well as from the point of view of deposited layer diagnostics.

As mentioned, the chamber was equipped with two 3“magnetrons in positions with perpendicular axis as shown on the figure 4-2. Both of them had inserted ITO targets. The bottom magnetron was operated in pulsed regime close to HiPIMS. The upper was supplied by RF source (13.56 MHz). The experiments were carried out typically with reactive N_2/Ar atmosphere. As a substrate, glass pieces and silicon wafers were used. The substrate was placed on the rotational table under the RF magnetron.

This study aimed to describe primarily the following three areas of interest:

A. A dependence of the deposition process on a pressure
B. An influence of an average current delivered by HiPIMS magnetron
C. An influence of a nitrogen presence in the deposition process

5.1 Experimental setup

The experimental setup will be described in this part.

5.1.1 The influence of pressure

RF magnetron: Power P = 300W

HiPIMS magnetron: Current I_m = 0.78 A
Voltage $U \approx$ 470 V
Frequency f = 1 kHz
Duty cycle s = 10 %

Deposition atmosphere: Argon flow Ar = 15 sccm
Nitrogen flow N_2 = 0.2 sccm

The influence of the pressure was tested.

5 experiments with different pressure were performed:

1) p = 0.5 Pa
2) p = 0.9 Pa

3) p = 1.3 Pa
4) p = 1.7 Pa
5) p = 2.1 Pa

5.1.2 The influence of HiPIMS current

RF magnetron: Power P = 300W

HiPIMS magnetron: Voltage $U \approx 470$ V

Frequency f = 1 kHz

Duty cycle s = 10 %

Deposition atmosphere: Pressure p = 0.5 Pa

Argon flow Ar = 15 sccm

Nitrogen flow N_2 = 1 sccm

The influence of the HiPIMS current was tested.

5 experiments with different HiPIMS current or RF power were performed:

1) HiPIMS turned off, RF P = 300W
2) HiPIMS I_m = 0.195 A, RF P = 300W
3) HiPIMS I_m = 0.39 A, RF P = 300W
4) HiPIMS I_m = 0.78 A, RF P = 300W
5) HiPIMS I_m = 0.78 A, RF turned off

5.1.3 The influence of a nitrogen

RF magnetron: Power P = 300W

HiPIMS magnetron: Current I_m = 0.78 A

Voltage $U \approx 470$ V

Frequency f = 1 kHz

Duty cycle s = 10 %

Deposition atmosphere: Pressure p = 0.5 Pa

Argon flow Ar = 15 sccm

The influence of the Nitrogen flow was tested.

5 experiments with different nitrogen flow were performed:

1) N_2 = 0 sccm
2) N_2 = 0.1 sccm
3) N_2 = 0.2 sccm
4) N_2 = 0.4 sccm
5) N_2 = 0.8 sccm

5.2 Results of the experiments

5.2.1 Properties of plasma discharges used for deposition of ITO thin films

It was already mentioned that ITO thin films were deposited by co-sputtering of two magnetrons, both equipped by an ITO target. The sputtering guns were oriented perpendicularly as shown in figure 4-2. One discharge was driven with RF power P_{RF} = 300 W operated at frequency f_{RF} = 13.56 MHz. The waveform of RF discharge used during the deposition is shown in figure 5-1.

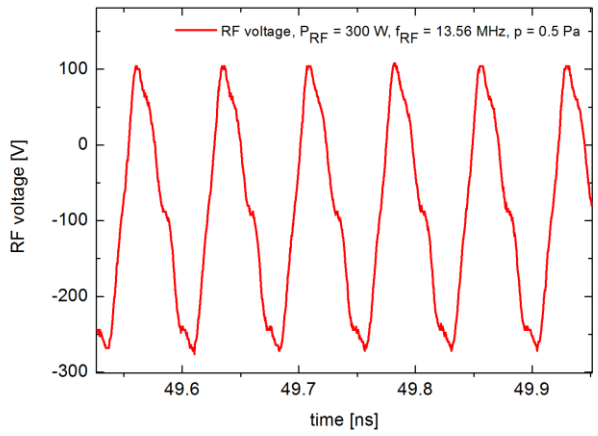

Figure 5-1 Voltage waveform of RF discharge running at P_{RF} = 300 W, f_{RF} = 13.56 MHz and process pressure p = 0.5 Pa, which represents typical deposition condition.

The voltage was measured directly on the driven electrode, i.e. ITO target, by a high voltage probe observing the waveform on a digital oscilloscope. The sinusoidal waveform displaces to a negative voltage which indicates so-called *dc offset voltage* (~125 V). The target has acquired a self-bias, which in this case has a value equal to nearly half the applied RF peak-to-peak voltage. It means that the applied voltage has a positive value only for a short fraction of each cycle, and ion bombardment of the target (bombardment by positive ions) is almost continuous and efficient.

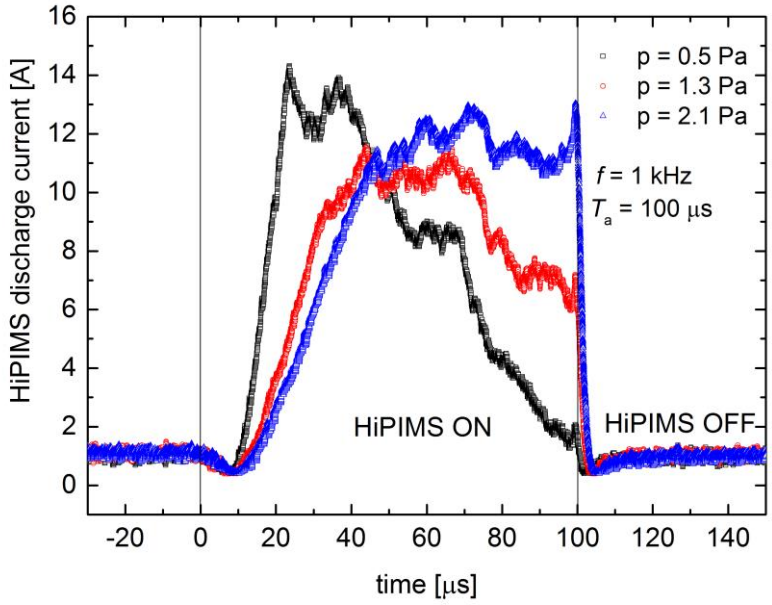

Figure 5-2 HiPIMS waveforms of discharge driven with repetition frequency f = 1 kHz, duty cycle 10% and mean discharge current I_m = 780 mA. Pressure as a parameter was changed within a range 0.5 – 2.1 Pa. Two vertical lines at 0 and 100 μs show start and end of the control pulse.

Figure 5-2 shows HiPIMS discharge waveforms and their dependence on process pressure *p*. It should be reminded that there was the same mean discharge current for all measurements that are presented in figure 5-2. It is evident that the discharge current starts to rise with a small delay of 10 μs after the pulse onset. Since the voltage applied on the cathode was of rectangular shape with a minimal delay (observed delays ≤ 1 μs) this behaviour is considered to be physical effect. It might be caused by the presence of RF plasma generated by continuously running "second" magnetron. Furthermore, it is evident that pressure in the deposition chamber significantly influences the shape of HiPIMS waveforms. The current for low pressure discharge $p \approx 0.5$ Pa rises quite quickly and reaches its maximum $I_p \approx 12$ A at roughly 20 μs. Such peak discharge current correspond with peak power density about 280 W.cm^{-1}. Current drop, observed after reaching its maximum, is typical for HiPIMS metallic discharges and is usually explained by a gas rarefaction effect. Gas rarefaction in the target vicinity is caused by so-called sputtering wind (i.e. process when sputtered particles push away gas atoms in close target neighbourhood) and by thermal heating of the cathode / target. None of these effects should be neglected in our case because of high mean discharge current I_m = 780 mA. It should be also noted that RF waveforms are only slightly influenced by pressure; it is mainly the dc offset voltage $|V_{off}|$ which decreases with growing pressure.

At higher pressure the rarefaction effect is vanishing and the current fall is not so obvious. It is well pronounced for waveform measured at p = 2.1 Pa in figure 5-2 where a current plateau is distinguishable. The reduction of gas rarefaction effect is attributed to larger number of species in the discharge volume; the number of species is proportional to pressure. This shape of discharge current is usually observed during reactive HiPIMS of e.g. metal oxide films. In reactive sputtering, the current rise is explained by enhanced emission of secondary electrons from compound layer on the target surface. This phenomenon could also play a role in this case since a compound target In_2O_3/SnO_2 of composition 90/10 is sputtered.

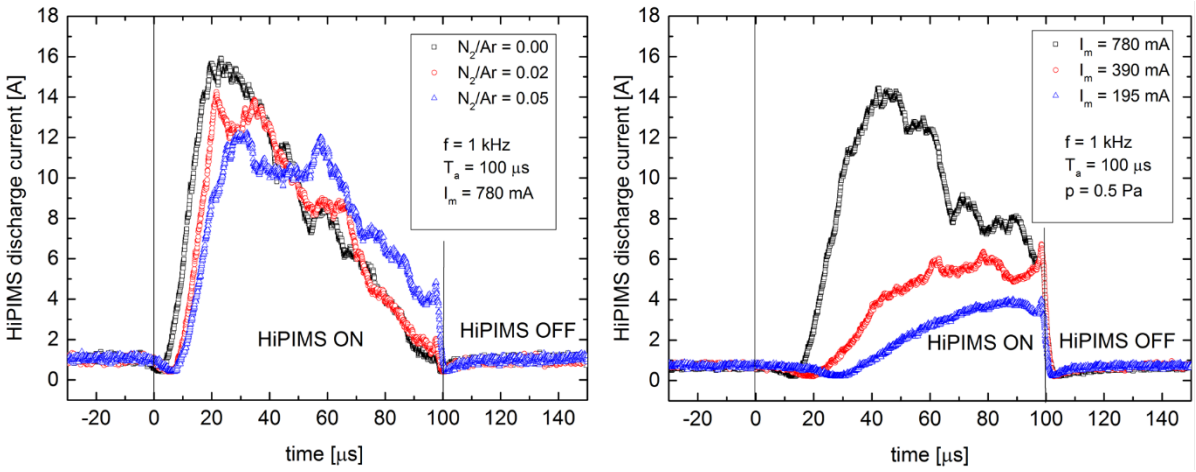

Figure 5-3 HiPIMS waveforms for different gas composition (left panel) and different mean discharge current (right panel).

However, results presented in figure 5-3 indicate that the gas rarefaction is the main mechanism which determines waveform shape of HiPIMS. Left panel of figure 5-3 demonstrates that the gas composition does not influence the current significantly. In this case the discharge was running with the highest mean current I_m = 780 mA and low pressure p = 0.5 Pa: as a result, waveform shapes, typical for gas rarefaction, occur. Also, it should be highlighted that the reactive gas composition was rather weak $N_2/Ar \leq 0.06$ while the target composition has even higher amount of incorporated oxygen since In_2O_3/SnO_2 = 90/10 target were used. On the other hand, right panel of figure 5-3 represents HiPIMS waveforms measured for different mean currents I_m = 195, 390 and 780 mA, respectively. It is clearly demonstrated that for less intensive discharges when I_m = 195, 390 mA the current fall does not occur, while it is significant for I_m = 780 mA indicating gas rarefaction caused by an intensive sputtering at high mean current.

5.2.2 Optical emission spectroscopy

Optical emission spectroscopy is an efficient tool for diagnostics of chemical (elemental) composition and behaviour of plasma discharges. In our case plasma properties were revealed in the substrate vicinity, i.e. the optical fibre was inserted inside the vacuum chamber and faced towards the substrate. The motivation of this diagnostics was to study processes in the substrate region which might influence deposition process. Special attention was paid to diagnostics of emission spectral lines of metal species. Hence, from the overview spectra in figure 5-4, these dominant lines were chosen: In (450.9 nm), In^+ (591.0 nm), Sn (283.6 nm) and Sn^+ (607.5 nm), respectively.

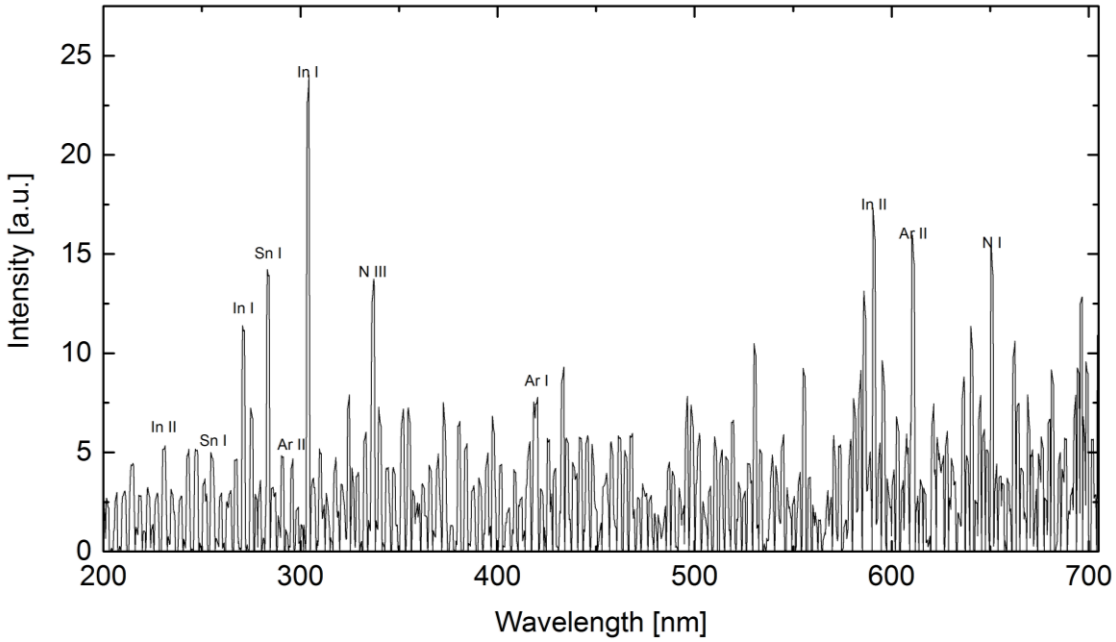

Figure 5-4 Overview of emission spectra measured in the substrate vicinity. Plasma discharge was produced by co-sputtering of HiPIMS (f = 1 kHz, T_a = 100 µs, I_m = 780 mA) and RF (P_{RF} = 300 W) discharges driven in atmosphere N_2/Ar = 0.06, p = 0.5 Pa.

Since the spectrograph was equipped by an iCCD camera the time resolved measurements were performed with a time step of 5 µs. Time-resolved measurements, performed for In (450.9 nm), are shown and compared for HiPIMS and HiPIMS+RF discharges in figure 5-5. Here, axis *x* represents the wavelength, *y* denotes time and *z* is the emission intensity. The left panel in figure 5-5 shows the intensity evolution in single running HiPIMS discharge, i.e. with RF discharge off. The intensity maximum is reached at about of 50 - 75 µs after the pulse onset followed by its drop. This well corresponds with behaviour of the discharge current, see left panel of figure 5-3. Hence, it is assumed that fall of the discharge current, explained by gas rarefaction, might be also responsible for reduced sputtering effect in the

second half of the HiPIMS pulse. This behaviour is expected as unwanted because reduced sputtering decreases deposition rate.

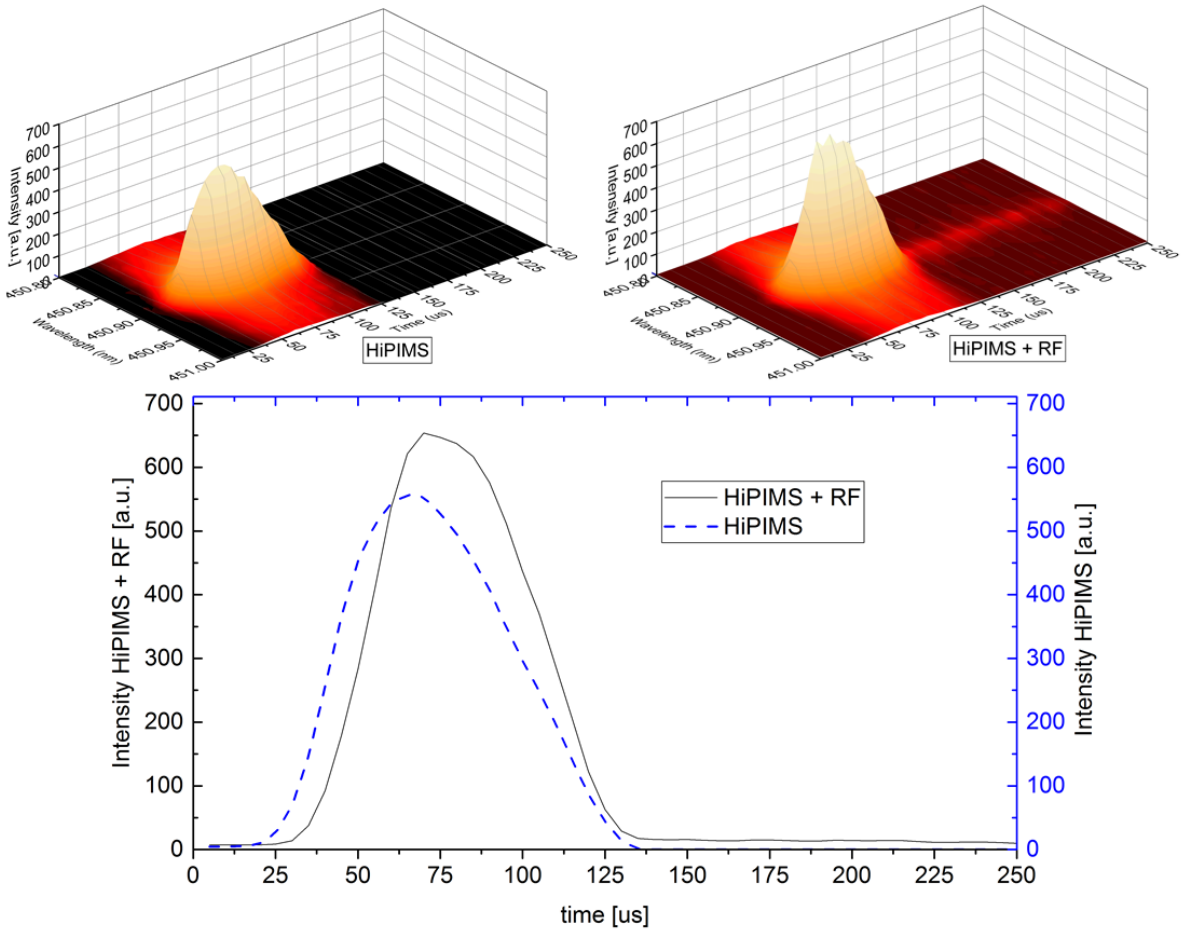

Figure 5-5. Comparison of time evolution of In (450.9 nm) emission intensity for HiPIMS (upper left panel) and HiPIMS+RF (upper right panel). Discharges were driven at the same experimental conditions f = 1 kHz, T_a = 100 μs, I_m = 780 mA in atmosphere N_2/Ar = 0.06, p = 0.5 Pa without and with RF (P_{RF} = 300 W) magnetron sputtering. The bottom panel compare the line peak intensity development in time.

The right panel of figure 5-5 demonstrates the effect of RF discharge on the time evolution of In (450.9 nm) emission line. First of all, enhanced emission intensity, which can be somewhat considered proportional with sputtering rate, was observed. Furthermore, culmination of the intensity was observed later with slightly postponed fall of the intensity. After HiPIMS pulse end, i.e. in time $\tau \geq 100$ μs, significantly lower, but still easily recognizable, emission at the same wavelength can be observed which is produced by RF discharge continuously running during the HiPIMS idle time. Despite not knowing exactly complete excitation mechanisms it is considered that major part of In deposited species is produced during HiPIMS pulses keeping in mind differences between intensities measured inside and outside of the HiPIMS pulse width and fact that duty cycle rather high 10 %.

Description of time-resolved measurements presented above was related only to one particular line, In (450.9 nm). However, similar behaviour can be confirmed also for another λ which are attributed to metal and metal ion species.

Intensities measured at each peak maximum were selected and are presented as dependencies on input process parameters for further evaluation of discharge properties. For example, dependence of emission intensity on the process pressure p is shown in figure 5-6. It is evident that intensities of metals (In, In^+, Sn, Sn^+) increase more or less proportionally with pressure. It is assumed that emission intensity is somewhat proportional to number of excited species which are subsequently proportional to the number of sputtered species. In other words, dependences in figure 5-6 indicates rise of number of deposited species with increasing pressure. This is rather surprising because number of species, arriving to the substrate region, should decrease due to elastic collisions and diffusion inside the discharge volume. This unexpected behaviour might relate to gas rarefaction effect caused by intensive HiPIMS at I_m = 780 mA. It was already mentioned above that emission intensity corresponds with discharge current waveforms, compare figure 5-6 and figure 5-5. Gas rarefaction, indicated by fall of the discharge current, prevents (mainly) gas Ar^+ atoms to bombard a target surface and to provide efficient sputtering and production of deposited species. Hence, the total number of sputtered species is reduced at lower pressures which also results in weaker emission intensity. Such explanation is supported by the fact that rise of intensities was observed for metal atoms (In, Sn) as well as metal ions (In^+, Sn^+). On the other hand, the intensity of Ar^+ (376.6 nm) behaves contrary, i.e. decreases with increasing pressure. One can understand it because population of metal species rises with subsequent possible ionization due to low ionization potentials In^+ 5.78 eV, Sn^+ 7.34 eV as indicated by figure 5-6. Hence, the preferential ionization of metal species causes lack of energetic species (electrons and/or metastable Ar^*) suitable for Ar excitation.

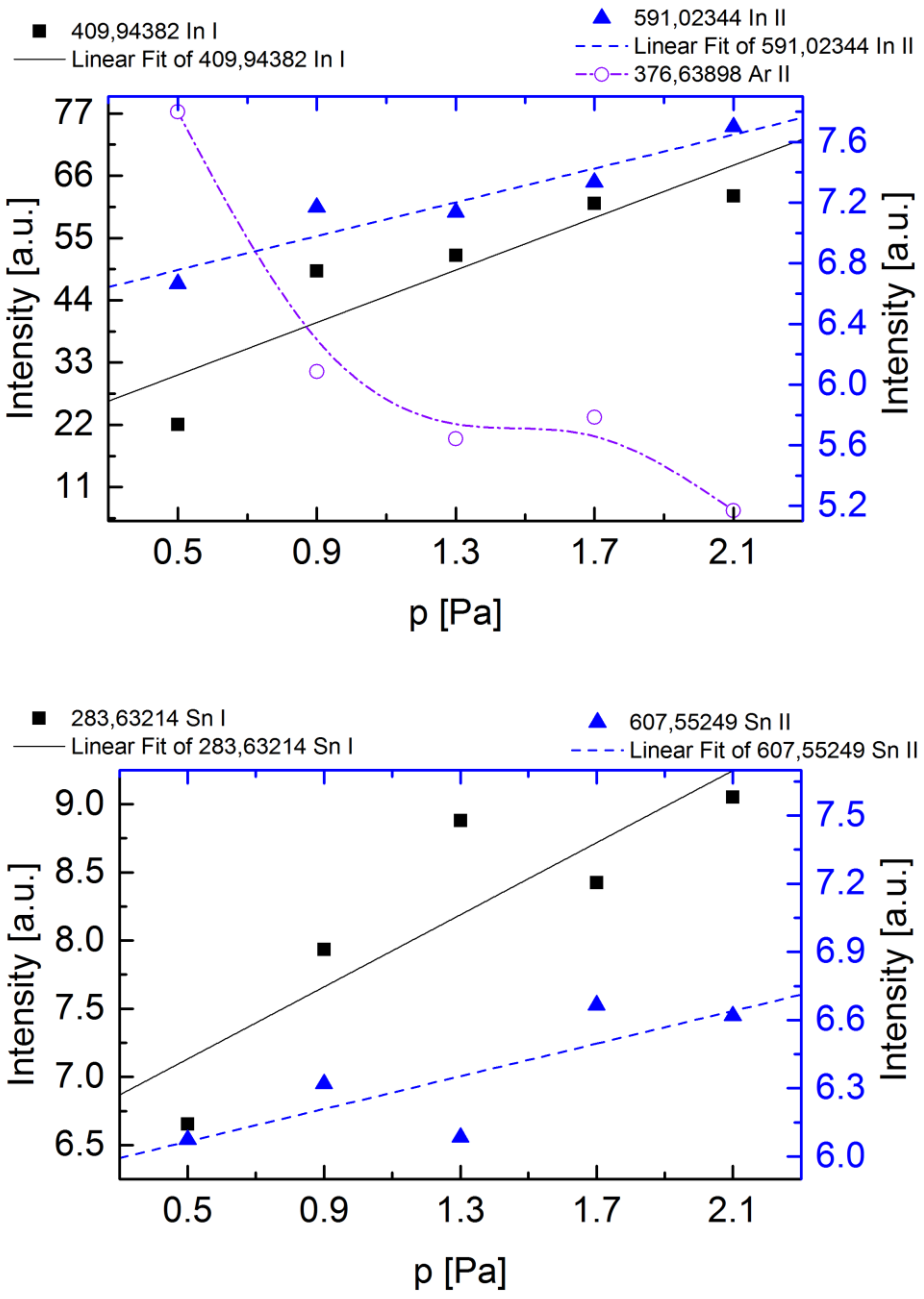

Figure 5-6 Dependence of emission intensity for selected spectral lines In (409.9 nm), In^+ (591.0 nm), Sn (283.6 nm), Sn^+ (607.6 nm) and Ar^+ (376.6 nm) on process pressure p. Intensity was measured for HiPIMS+RF discharge (HiPIMS: f = 1 kHz, T_a = 100 µs, I_m = 780 mA, RF: P_{RF} = 300 W) in atmosphere N_2/Ar = 0.01.

Reactive gas N_2 added into the discharge decreases the emission intensity, see figure 5-7. Decrease of emission intensity of sputtered species in reactive discharges is usually explained by formation of a compound layer on the target surface which reduces sputtering rate, so called *target poisoning*. However, the target poisoning may not be the main actor in our case. First, the intensity drop is recognizable even with small amount of added N_2, $N_2/Ar \leq 0.03$. Such amount is nearly negligible especially if compound target

In_2O_3/SnO_2 = 90/10 is used. It is obvious for Sn (285.6 nm) when intensity is reduced about of 50 %. On the other hand, decrease of In (450.9 nm) intensity is slower and less significant (about of 15 %). Observed difference is of course influenced by different sputtering yields that are reported Y_{In} = 2.1235 and Y_{Sn} =1.569 for Ar^+ bombardment at 600 eV. It can explain why emission intensity of material with lower sputtering yield drops quickly. Because the discharge waveforms do not suffer by reactive gas admixture significantly (see left panel of figure 5-3) it is assumed that production of sputtered species is namely influenced by elemental processes in the discharge volume. Bound dissociation energy of N_2 molecule is high 9.79 eV as well as ionization potential of nitrogen atom 14.54 eV. Despite these energies are higher than the ionization energies of metals (In and Sn) they are lower than the ionization potential of Ar 15.76 eV. By another words N_2 dissociation and N ionization most probably reduces number of Ar^+ which are responsible for sputtering of metal species. In the same graph the dependence of emission intensity of N^{++} (336.7 nm) is shown, too. It is not so surprising that the intensity rises with increasing N_2/Ar ratio.

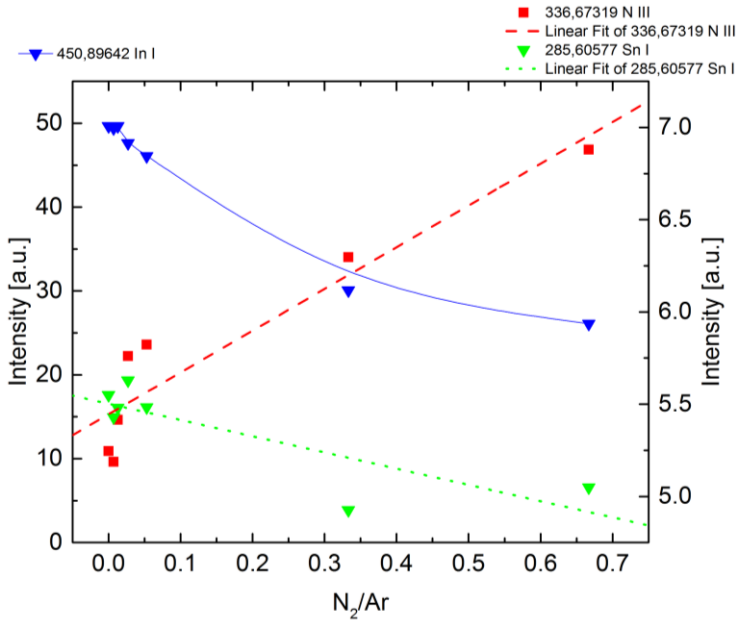

Figure 5-7 Dependence of emission intensities for In (450.9 nm), Sn (285.6 nm) and N^{++} (336.7 nm) as a function of N_2/Ar ratio. Intensity was measured for HiPIMS+RF discharge (HiPIMS: f = 1 kHz, T_a = 100 µs, I_m = 780 mA, RF: P_{RF} = 300 W) at pressure 0.5 Pa.

The effect of HiPIMS mean current I_m to discharge properties was investigated too. Obtained results were more or less expected and support our previous explanations given above. Results are shown in figure 5-8. Intensity of Ar^+ (705.3 nm), indicating production of argon ions, increases with increasing HiPIMS discharge current. Easily, it is caused by enhanced energy density in the discharge volume and subsequent ionization of Ar atoms. Argon ions

bombard the target surface and produces free metal species that are deposited onto the substrate. Proportional dependence of all metallic lines (In, In^+, Sn and Sn^+) on discharge current was observed. It is also obvious that emission produced by single running RF discharge is the lowest for all measured cases and is further increased when HiPIMS discharge is activated.

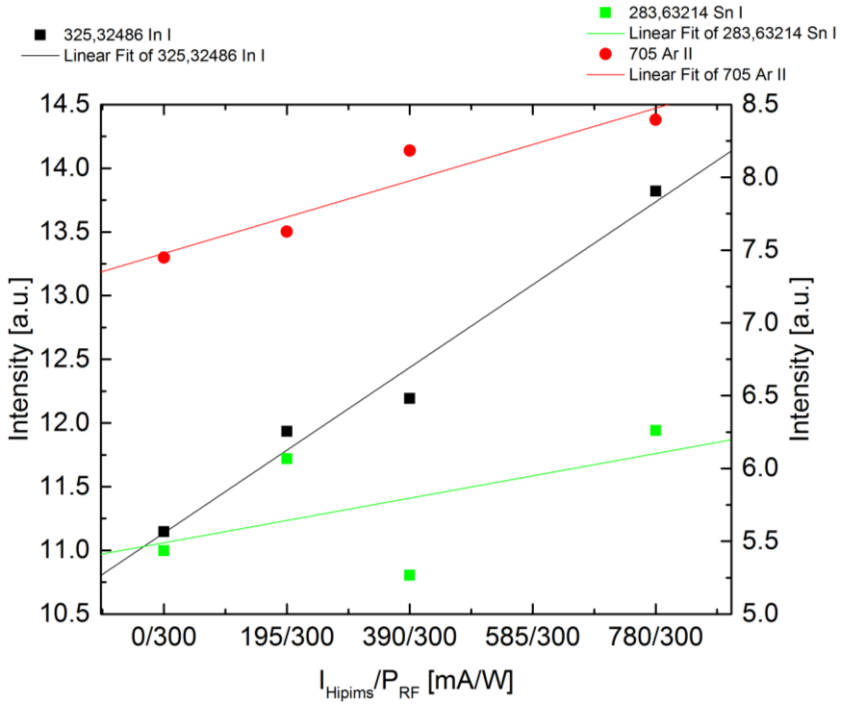

Figure 5-8 Dependence of emission intensities of In (325.3 nm), Sn (283.6 nm) and Ar^+ (705.3 nm) on mean HiPIMS discharge current. The first point, denoted as 0/300 on the x-scale, represents I_m = 0 mA, i.e. only single driven RF discharge was investigated. Other experimental parameters: (HiPIMS: f = 1 kHz, T_a = 100 µs, RF: P_{RF} = 300 W) at pressure 0.5 Pa.

5.2.3 Langmuir probe measurements

Langmuir probe measurements were carried out together with optical emission spectroscopy at the same time. Hence, the probe as well as optical measurements were performed at similar conditions. The probe was placed in the substrate region; to similar place the optical fibre was oriented, too. Comprehensive measurements of the magnetic field, by a Hall probe, in the probe position, confirmed low intensity of the field $B_{\parallel,\perp} \approx 0.1$ mT. Hence, the calculated Larmor radius is significantly larger than the probe size. From this reason an effect of the magnetic field on electron behaviour was fully neglected in the frame of this work. Furthermore, it should be reminded that all data were obtained in time-resolved mode with a time step of 3 µs. Than the particular plasma parameters (electron density n_e, electron temperature T_e and plasma potential V_{pl}) were determined using methods and formulas described in chapter 3. Once time-resolved dependences were obtained than their mean

values, calculated over the HiPIMS pulse, could be estimated. These mean values as a function of input process parameters are presented in graphs and discussed in the text below.

In figure 5-9, dependences of electron density n_e, electron temperature T_e and plasma potential V_{pl} on mean HiPIMS discharge current are shown. All these physical quantities exhibit the same trend: The highest values were observed for single driven RF discharge and decrease with increasing mean HiPIMS current. For following discussion, it should be kept in mind that obtained values were measured in the substrate region, i.e. about of 10 cm from the sputtered cathodes.

Relatively high plasma potential $V_{pl} \approx 50$ V is typical for RF plasma discharges and was already observed several times. Usually, this effect is explained by enhanced electron diffusion towards the electrode or chamber wall. On the other hand, negative plasma potential was measured in HiPIMS discharges during the pulse. Negative potential is caused by large number of secondary electrons that are emitted from the target after intensive striking of bombarding ions. Hence, it is assumed that HiPIMS contribution (better to say its negative V_{pl}) results in decrease of plasma potential in the substrate space.

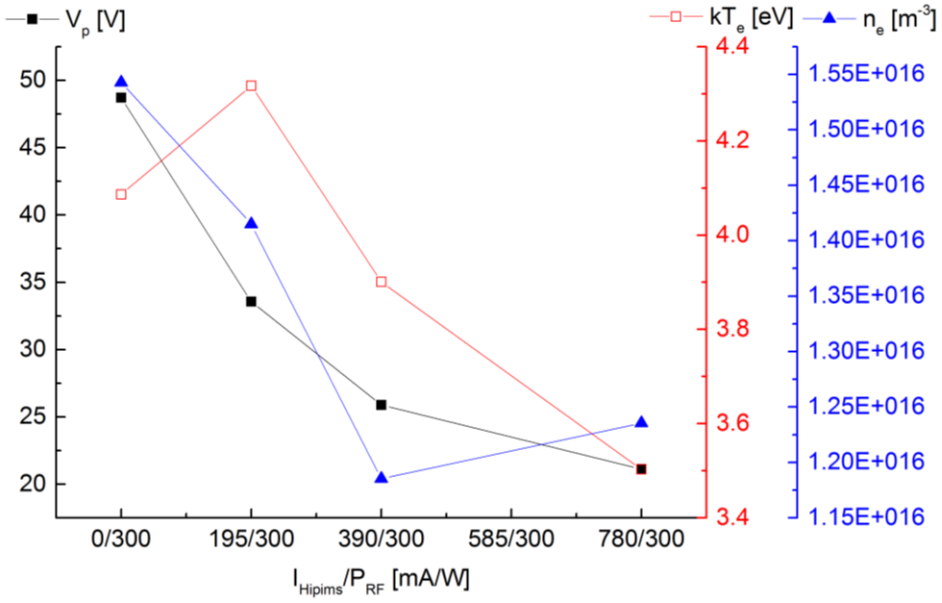

Figure 5-9 Dependence of electron density n_e, electron temperature T_e and plasma potential V_{pl} on mean HiPIMS discharge current. The first point, denoted as 0/300 on the x-scale, represents $I_m = 0$ mA, i.e. only single driven RF discharge was investigated. Other experimental parameters: (HiPIMS: $f = 100$ Hz, $T_a = 100$ µs, RF: $P_{RF} = 300$ W) in reactive atmosphere $N_2/Ar = 0.06$ at pressure 0.5 Pa.

Behaviour of electron density is similar, as already mentioned. Electron density was estimated $n_e \approx 10^{16}$ m^{-3} which well corresponds with expected values for RF discharges. One could expect higher n_e absolute values for HiPIMS where $n_e \approx 10^{18}$ m^{-3} are easily achievable. However, it should be kept in mind that in our case not only HiPIMS frequency

f_{HiPIMS} = 1 kHz but mainly the duty cycle 10% were higher. Such input parameters are responsible for reduced electron densities. Decrease of n_e might be caused by enhanced ionization of sputtered species nearby the substrate. It is indicated by figure 5-8 that number of sputtered and ionized species rises with increase of HiPIMS discharge current. However, sputtering of metal atoms and their subsequent ionization is a dominant process in near-cathode region. Here electrons lose their energy, due to inelastic collision with atoms, and are caught by the magnetic field. It is also important to mention that despite obvious drop of n_e the relative change is not so dramatic, just about of 40 %. This well corresponds with energy of electrons: $T_e \approx 4.2$ eV was measured for single driven RF discharge and dropped down to values $T_e \approx 3.4$ eV when HiPIMS is involved to the process with high I_m. This reduction is explained by energy loss during ionization of sputtered metal species.

Figure 5-10 shows dependences of electron density and electron temperature on process pressure. Apparently n_e rises proportionally with pressure which is the most probably caused by two facts: (i) number of (gas) species is proportional with pressure and its growth also increases ionization probability of gas atoms and (ii) the number of metal ions rises with pressure too, see figure 5-6, where electrons occurs as a product of ionization process. It seems like pressure difference about one order of magnitude is responsible for double change of electron density. Behaviour $T_e(p)$ supports this explanation since the electron energy drops to lower values significantly. It is expected that these energy losses are caused by ionization of sputtered species. Looking on the trend of measured data $T_e(p)$ one could argue that the first point (T_e = 7 eV) is rather a computational error than a result. However, it is believed that it is correct since the $V_{pl}(p)$ corresponds with $T_e(p)$ precisely. Energy drop is quite fast within a reaching pressure close to 1 Pa and become more or less constant afterwards. Observed plateau $T_e(p \geq 1$ Pa) is somewhat comparable with $n_e(p \geq 1$ Pa) where the rise of electron density is not so significant. This might relate to our former explanation of rarefaction effect on discharge properties. A noticeable transition between “metallic” and “poisoned” mode of sputtering at pressure around 1 Pa was observed during measurement of discharge current waveforms, see also figure 5-6.

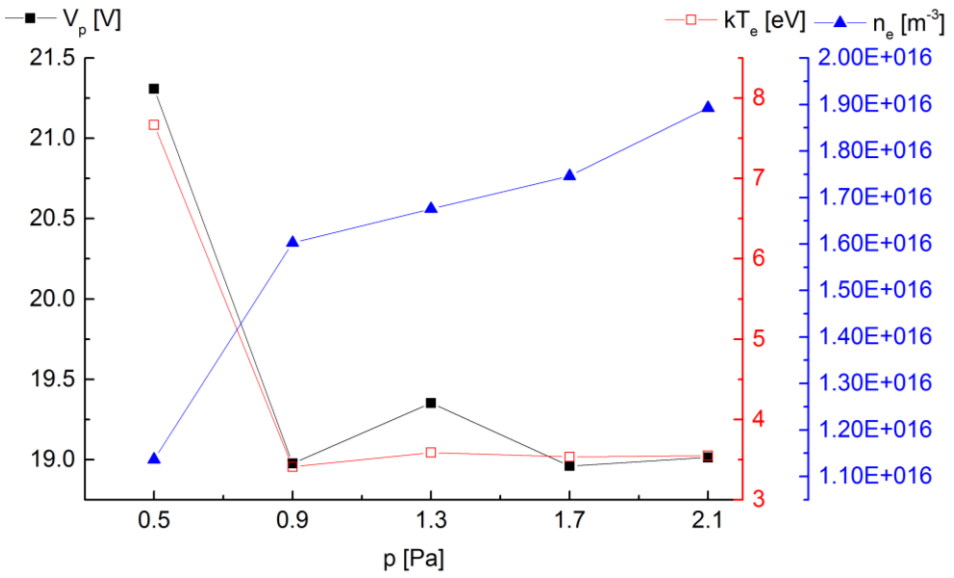

Figure 5-10 Dependence of electron density n_e, electron temperature T_e and plasma potential V_{pl} on process pressure p. Experimental parameters: (HiPIMS: f = 100 Hz, T_a = 100 µs, I_m = 780 mA, RF: P_{RF} = 300 W) in reactive atmosphere N_2/Ar = 0.01.

In frame of this work plasma parameters were investigated on the dependence of ratio N_2/Ar, too. Generally expected behaviour of studied plasma system was observed (not presented here as a graph). Plasma potential and electron temperature decrease with rising reactive ratio N_2/Ar. It is probably caused by the formation of a compound film on the target at $N_2/Ar \geq 0.3$ where reactive gas represents more significant part of gas mixture. Furthermore, delivered N_2 introduces another gas which, at least partially, is dissociated and ionized as indicated by figure 5-7. These are energy demanding processes which results in decrease of electron temperature. On the other hand, strong influence of $n_e(N_2/Ar)$ was not observed. Nearly negligible rise of n_e might be caused by ionization of nitrogen atoms in the discharge volume since the ionization potential of N (14.5 eV) is still lower than of Ar (15.7 eV).

5.2.4 Effect of total pressure in the chamber

The effect of total pressure *p* in the vacuum chamber on layer was investigated first. For that reason, the pressure was varied in range *p* = 0.5 – 2.1 Pa. The XRD patterns measured for film prepared at *p* = 0.5 Pa and *p* = 2.1 Pa are compared in figure 5-11. For both cases, well crystalline $In_xSn_yO_z$ was observed however with preferred orientation along [h00]. As shown in figure 5-11, higher pressure film indicates more pronounced [h00] preferred orientation and the complete diminishing of the x-ray amorphous parts (28-30 °) in comparison to the low-pressure film.

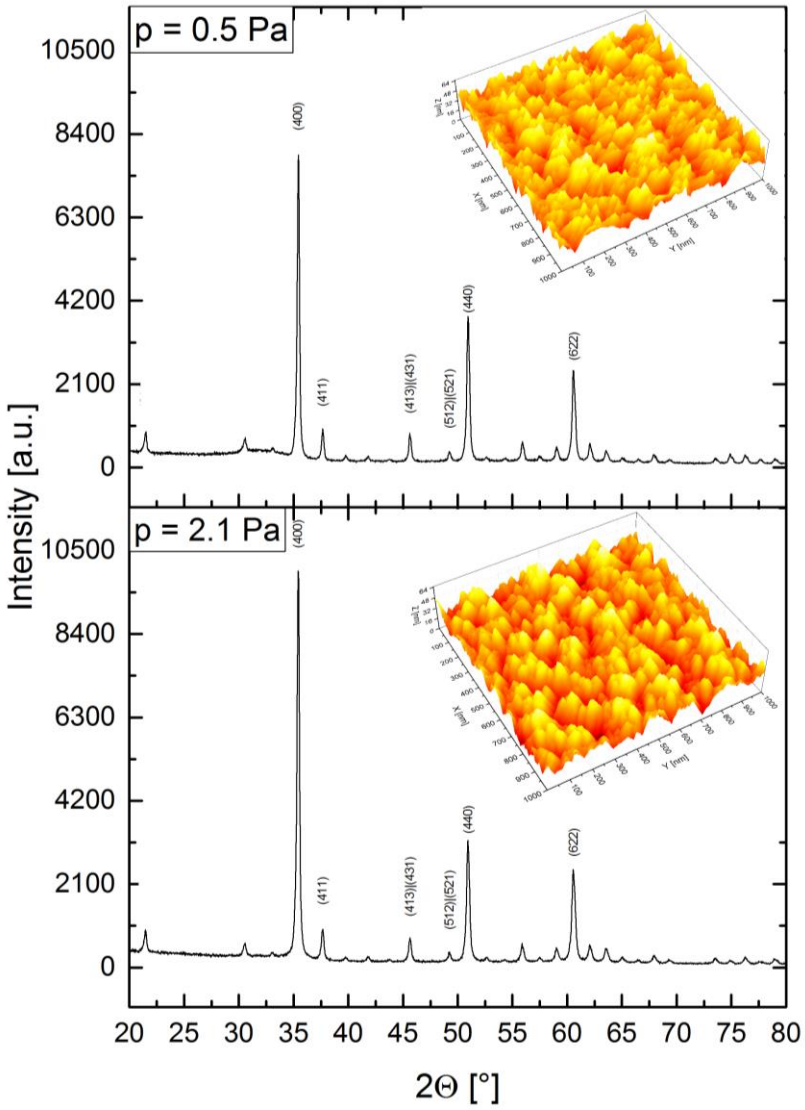

Figure 5-11 XRD patterns of ITO films deposited at different pressures: upper panel p = 0.5 Pa, lower panel p = 2.1 Pa. Both films were deposited by HiPIMS+RF discharge driven with mean HiPIMS current I_m = 780 mA and RF power 300 W. Gas mixture N_2/Ar = 0.01 was used. Immersed images represent surface morphology measured by AFM.

The immersed AFM images illustrate the surface morphology of deposited films. A surface roughness σ_{rms} as a function of pressure p is shown in figure 5-12. Some small rise of the surface roughness was observed. It seems to be nearly proportional to the pressure with observable plateau for $p > 1.5$ Pa. Smoother surfaces $\sigma_{rms} \approx 5.6$ nm measured for $p = 0.5$ Pa is caused by a bombarding effect of deposited species which arrives onto the substrate with higher energy. Mean free path λ calculated for low pressures is about of $\lambda \geq 10$ cm $\approx d$, here d denotes the distance target vs. substrate. Hence, sputtered particles impinging the substrate without collision having a Thompson energy distribution of sputtered particles. At pressure $p > 0.5$ Pa sputtered particles starts to collide in the discharge volume and their energy is depleted resulting in formation of surfaces with higher roughness and an enhanced epitaxial crystallite growth. Altought the rise of the film roughness is apparently linear, small absolute values σ_{rms} should be reminded.

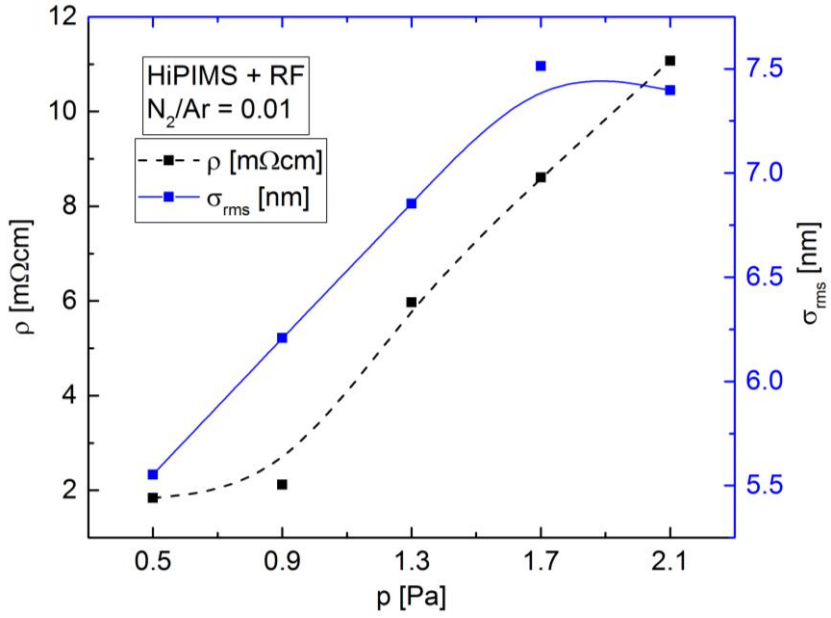

Figure 5-12 Dependence of ITO film resistivity (right scale) and surface roughness (left scale) on working pressure in the chamber. Films were deposited by HiPIMS+RF discharge driven with mean HiPIMS current I_m = 780 mA and RF power 300 W. Gas mixture N_2/Ar = 0.01 was used.

The dependence of the film electrical resistivity is shown in figure 5-12, too. It seems that the electrical resistivity ρ depends nearly linearly on the pressure. This trend is rather strong and shows that changes of pressure in frame of one order of magnitude can induce resistivity difference in the same range. Generally, it can be asserted that we are able to reach resistivity about of $\rho \approx 2$ mΩ.cm. This $\rho(p)$ predicates the method for tunable deposition of ITO films with ρ in a wide range.

5.2.5 Effect of HiPIMS contribution

It should be reminded that results obtained and presented in figures 5-11 and 5-12 belong to film deposited in reactive N_2/Ar atmosphere and using combined HiPIMS and RF sputtering. The effect of HiPIMS contribution to the deposition is illustrated in figure 5-13.

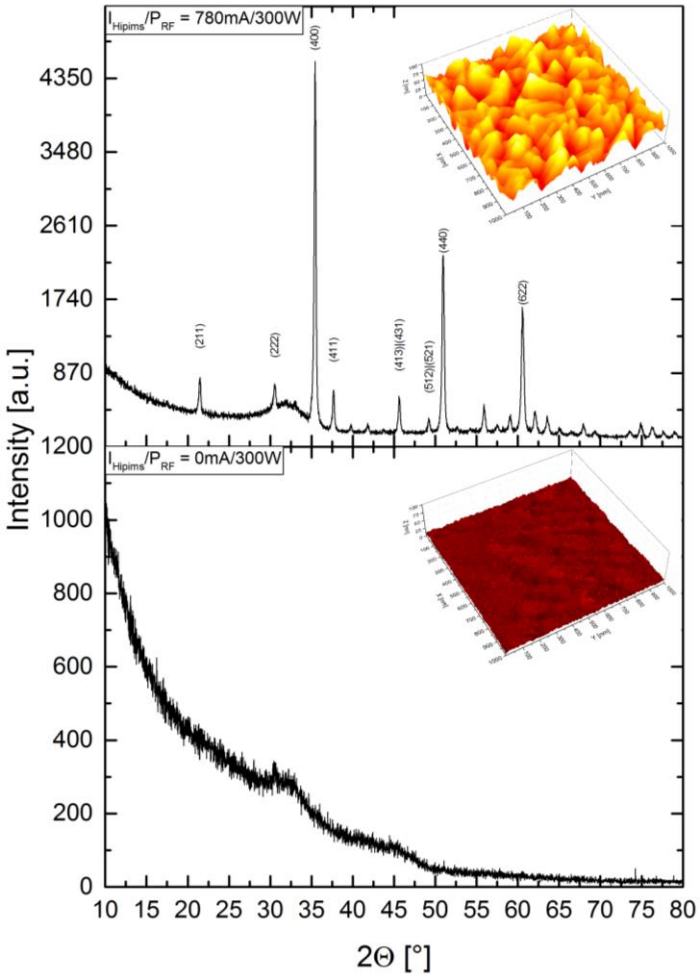

Figure 5-13 Comparison of XRD patterns and AFM images of films deposited using RF+HiPIMS (upper panel) and RF (lower panel). Films were deposited by RF+HiPIMS discharge driven with mean HiPIMS current I_m = 780 mA and RF power 300 W. Gas mixture N_2/Ar = 0.06 was used. Smooth and x-ray amorphous films were prepared by RF discharge.

The figure compares XRD patterns for HiPIMS+RF and only RF discharge. The HiPIMS+RF patterns reveal well crystalline structure with preferred orientation [h00] while the film deposited by RF discharge are mainly x-ray amorphous with only one Bragg peak at 30.6 °/2θ. This peak corresponds to the (222) Bragg reflection, the most intensive peak in the

ITO x-ray pattern if the crystallites are statistically distributed. Furthermore, the effect of added HiPIMS discharge on film crystallinity was examined by subsequent increase of HiPIMS discharge mean current in range of I_m = 0 – 780 mA. It is apparent again that a [h00] preferred orientation together with crystallinity (increasing peak intensity in the x-ray pattern) increase with rise of the HiPIMS discharge power. It is also apparent from AFM image, inserted in figure 5-13, that the surface morphology is rather smooth with $\sigma_{rms} \approx 5$ nm, corresponding with roughness observed in figure 5-12, and somewhat decreases with less efficient HiPIMS discharges (not shown as a figure). The effect of improved crystallization is attributed to enhanced energy delivery to the growing film.

Figure 5-14. shows the dependence of ITO electrical resistivity ρ on HiPIMS discharge power. Point α in figure 5-14 represents the resistivity of the film prepared by RF driven discharge, where $\rho \approx 2.18$ mΩ.cm. It is obvious that RF discharge results in formation of ITO films with the lowest resistivity. This behaviour is unexpected because high resistivity is typical for amorphous films. Hence, it is assumed that the film is rather nanocrystalline with size domain below the x-ray detection limit. Effect of low ρ for nanocrystalline structure is not fully understood yet and needs to be investigated. It is apparent that domains in film prepared with HiPIMS contribution, e.g. film δ (in figure 5-14), are larger and their resistivity is higher reaching the values about of $\rho \approx 7.18$ mΩ.cm. Hence, the effect of relatively high electric conductivity for α film prepared by RF might be caused by tunnelling effect of conducting electrons moving through the small particles. In case of larger domains, formed due to energy contribution of HiPIMS discharge, the electron movement is expected to be along grain boundaries.

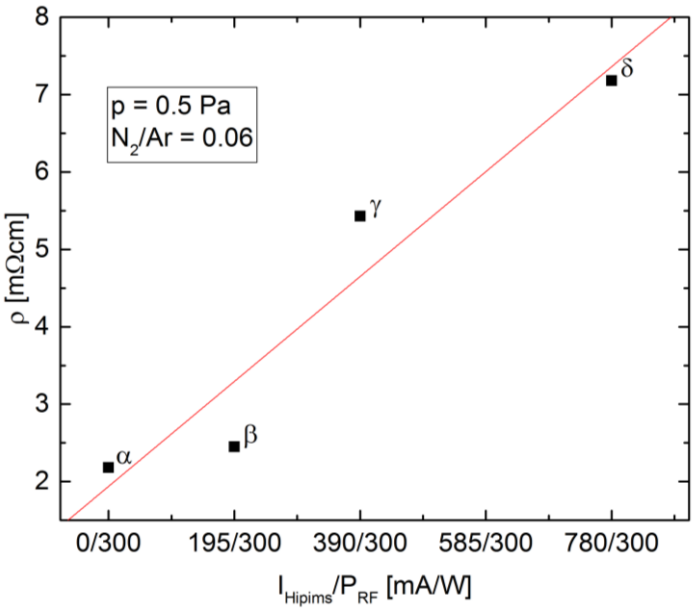

Figure 5-14 The dependence of ITO film resistivity on HiPIMS contribution to the deposition process. Gas mixture N_2/Ar = 0.06 and pressure p = 0.5 Pa was used.

Nearly ideally crystalline $In_xSn_yO_z$ structure with crystallites preferentially oriented along [h00] deposited by combined HiPIMS+RF discharges, see figure 5-11 and 5-13, is attributed to enhanced energy through HiPIMS contribution. The effect of energy on film crystallization was also studied by post deposition thermal annealing (at 400 °C for 120 min) of RF deposited films, i.e. annealing of α film from figure 5-14 which x-ray amorphous structure is shown in lower panel of figure 5-13. The annealing effect is illustrated by figure 5-15, where are compared x-ray patterns of HiPIMS+RF film and RF film after thermal annealing. As assumed, the peak intensities of RF annealed film were even higher than those measured for HiPIMS+RF patterns. The high crystallinity of the RF annealed film shows that the deposition procedure can form ITO films with low level of imperfections (interstices, dislocations, grain boundaries). The annealing procedure supports hypothesis, that very small (below the x-ray detection limit) ITO crystals (nanocrystals) serves as seeds which are converted to larger and more compact ITO crystals due to energy delivered during annealing. The second observation concerns the preferred orientation. After annealing the crystals exhibits (111) preferred orientation, but clearly different from all the other investigated crystalline ITO films with [h00] orientation. Hence, employing of HiPIMS discharge, it is possible to deposit well crystalline structure which cannot be easily attained by simple post-deposition thermal annealing.

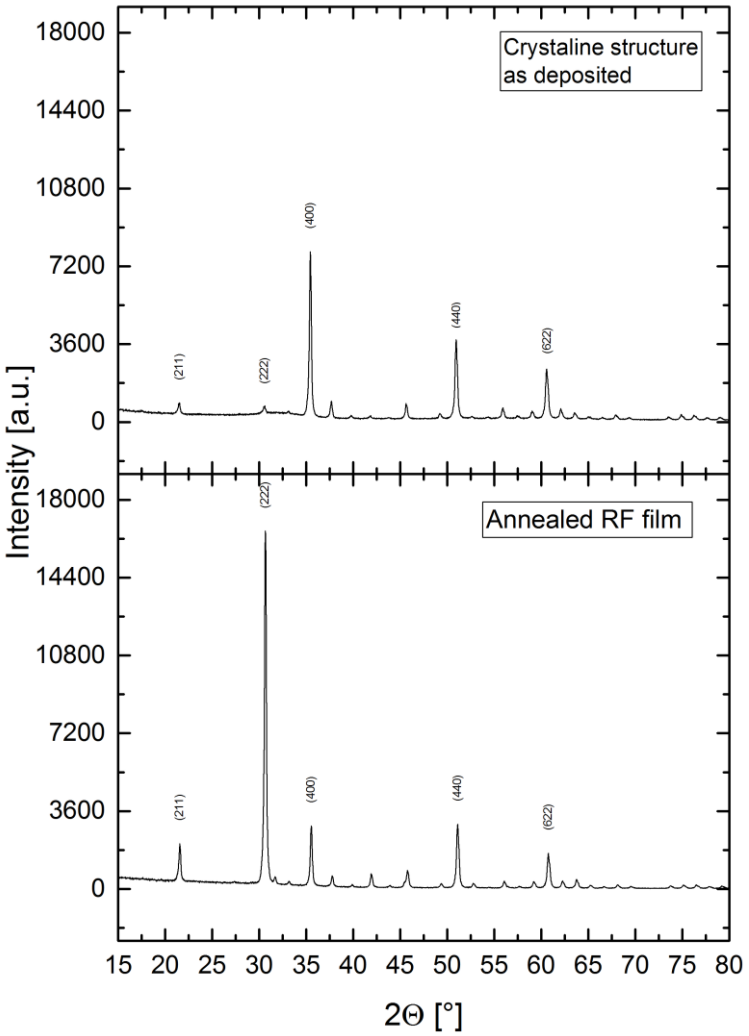

Figure 5-15 Effect of thermal annealing on ITO crystallography. Originally x-ray amorphous film (shown in lower panel of figure 5-3) become crystalline after annealing, see lower panel. For comparison, the x-ray pattern of HiPIMS+RF deposited film at low pressure is in the upper panel.

5.2.6 Effect of nitrogen added into the discharge

Another parameter which plays an essential role during ITO film formation is gas environment. Performed experiments show that addition of reactive N_2 into the discharge improves the ITO crystallization process. This effect was observed regularly and it is believed it is rather a physical effect than a random error. It is obvious from figure 5-16 where XRD pattern of ITO film deposited in pure Ar atmosphere is shown. No observable Bragg peaks indicate x-ray amorphous film; here it can be compared with XRD patterns in figure 5-11 and 5-13 which were deposited at similar conditions with reactive N_2. There are indicia, from the systematic measurements, that some saturation point for nitrogen partial pressure exists: the crystallinity is improved with rising nitrogen partial pressure up to

certain value. Further increase of N_2 partial pressure does not affect significantly the ITO crystallinity. It was already mentioned that the formation of crystalline and favourable ITO structure is most probably caused by higher mobility of deposited species during the deposition process. The x-ray pattern in figure 5-16 corresponds to the resistivity of sample A in figure 5-17. With rising N_2 partial pressure the films become better crystalline.

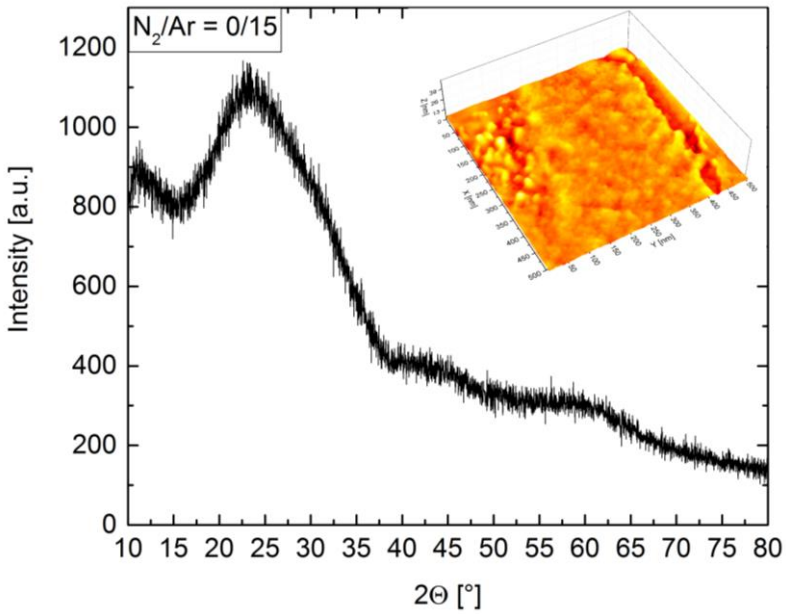

Figure 5-16 X-ray pattern of ITO film deposited in pure Ar atmosphere using HiPIMS+RF discharge (HiPIMS I_m = 780 mA and RF P = 300 W) running at p = 0.5 Pa.

Another important phenomenon connected with presence of nitrogen is introduced by possible preferential occupation of proper places of the lattice by nitrogen instead of oxygen. Such effect might result in enhanced electron density and subsequently improved electrical conductivity, i.e. reduced resistivity. It is demonstrated in figure 5-17, where resistivity decreases with increasing gas reactivity due to added nitrogen. In figure 5-17, the saturation point $N_2/Ar \approx 0.02$ under our experimental conditions can be observed. It seems that for $N_2/Ar > 0.02$ resistivity is not significantly influenced anymore and stays constant. On the other hand, no recognizable effect of nitrogen was observed neither on surface morphology nor σ_{rms} which was more or less independent on the N2/Ar ratio.

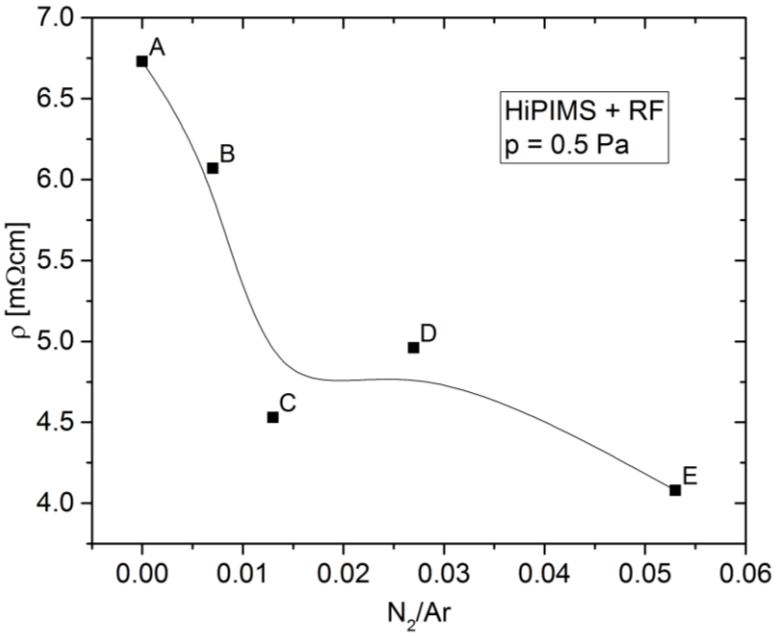

Figure 5-17 Dependence of ITO resistivity on mixture N_2/Ar. HiPIMS+RF discharge (HiPIMS I_m = 780 mA and 300 W) running at p = 0.5 Pa.

In this point, more attention should be paid to results shown in figure 5-12, 5-14 and 5-17 which seems to be contrary: in one case the resistivity decreases while in the second case the resistivity increases. First, it should be reminded that films presented in figure 5-14 were prepared with constant flow rate of reactive gas mixture N_2/Ar = 1/15 = 0.06, which is higher than expected saturation point at ratio N_2/Ar = 0.02 in figure 5-17. Hence, it is believed that formation of larger ITO crystals is conditioned by energy delivered to the growing film. Large crystals can be achieved also by post deposition thermal annealing, but different lattice orientation can be achieved. On the other hand, the film A (figure 5-17) was found x-ray amorphous and it is expected that the film is generally amorphous because of higher resistivity. This is exactly opposite with film α (figure 5-14) where the resistivity was measured $\rho \approx 2.18$ mΩ.cm which can be explained by nanocrystalline structure. Considering these results, it is assumed that the presence of nitrogen in the discharge volume improves and encourages the crystallization process due to substitution preferential reactions of nitrogen and due to energy contribution. Once the ITO crystals are formed, the electrical resistivity can be tuned due to their domain size, e.g. controlling the deposition process as shown in figure 5-12.

5.2.7 Film absorbance

High transparency and relatively low electrical resistivity introduce the main benefit of ITO films. It was shown in previous part that film resistivity can be easily tuned in range of a few orders of magnitude. Absorbance $\Lambda(\lambda)$ measured by UV-VIS spectrometry for films deposited at different pressures is shown in figure 5-18; here the upper panel shows full dependence for λ = 300 – 750 nm, while the lower panel details the dependences in range λ = 500 – 750 nm. Generally, it can be stated that transparency of deposited ITO films considered by a naked eye is high and from measured data can be estimated, using $\Lambda = \log(1/\Theta)$ where Θ denotes the film transparency, about of 80-95 % in visible and near infrared part of the spectrum.

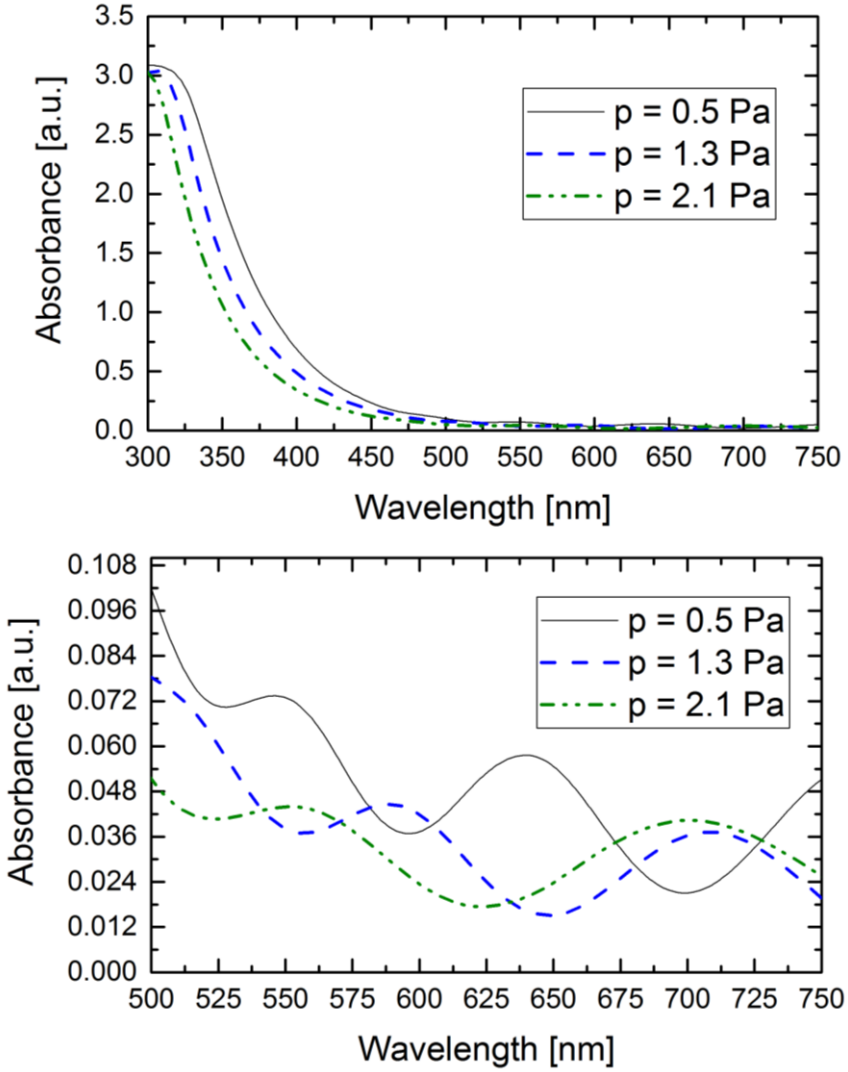

Figure 5-18 Behaviour of absorbance $\Lambda(\lambda)$ for ITO films deposited at different pressures. Films were prepared by HiPIMS+RF discharge in N_2/Ar = 0.01 gas environment.

However, it is obvious from figure 5-18 that Λ increases for λ < 450 nm. Increased absorbance in UV range is well known phenomena which is related with behaviour of heavily-doped-n-type semiconductor with a large band gap about of 3.5 – 4.3 eV. UV photons excite an electron from the valence band to the conduction band and the extinction coefficient *k* differs from zero. This energy losses of photons result in film opaque properties. Sometimes are reported also opaque ITO films in near infrared spectrum because of free carrier absorption, i.e. excitation of electron from near bottom to higher level within a conduction band similar to behaviour of metals.

Also, different $\Lambda(\lambda)$ for films deposited at different pressures were observed. It is evident that for e.g. $\Lambda(\lambda$ = 350 nm) the absorbance is low for film deposited at high pressure (p = 2.1 Pa), only about of 1%, while the absorbance is significantly higher for film deposited at low pressure (p = 0.5 Pa). It was proved that the film thickness was somewhat comparable, h = 480 nm ± 18 %, and the thickness differences were neglected; here it should be mentioned that the film thickness was measured by means of optical ellipsometry and mechanical profilometry giving us similar results. Similar effect is observable in figure 5-19 where are compared $\Lambda(\lambda)$ for films prepared by RF and RF+HiPIMS discharges. In this case the lower absorbance was measured for RF discharge deposited film. Comparing previously shown results for electrical resistivity and crystallographic properties, see Figs. 5-11 to 5-17, there is a trend which might explain $\Lambda(\lambda)$ behaviour. The lower the crystal imperfections in the films (interstices, grain boundaries) the higher is the absorbance in the low wavelength range. Higher $\Lambda(\lambda$ < 450 nm) was observed for smoother films. It is well known that films which exhibit increasing particle sizes become rough in their film surface. Hence, enhanced absorbance of UV-VIS spectrum could be also influenced by a surface morphology.

Details of $\Lambda(\lambda$ > 450 nm) for different pressures are shown in lower panel of figure 5-18. There are no dramatic differences of absorbance that are revealed within an error of a few percents. The absorbance is somewhat higher for well crystalline films deposited at low pressure. This effect was observed regularly. Despite not having an exact explanation for this effect the idea is that it is determined by film crystallinity and surface roughness.

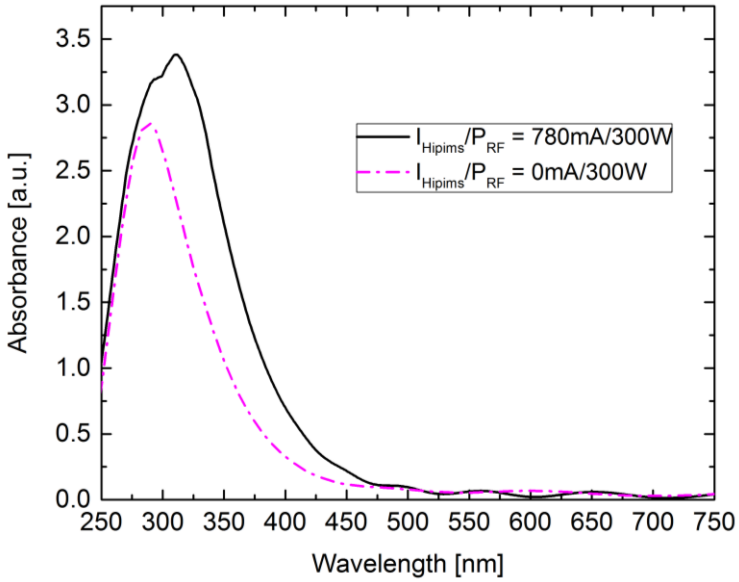

Figure 5-19 Comparison of absorbance $A(\lambda)$ for ITO films deposited with or without HiPIMS. Films were prepared in N_2/Ar = 0.06 gas environment at pressure p = 0.5 Pa.

6 Conclusion

In summary, experiments carried out demonstrates plasma as a promising tool for deposition of indium tin oxide (ITO). The research was mainly focused on development of the deposition methods and investigation of properties of deposited films. To study the film growth also the plasma diagnostics was performed. Provided experiments give a clear prove that optimization of the deposition process parameters determines properties of ITO films, e.g. its transparency, electrical resistivity, crystallinity as well as surface morphology.

Important step was incorporation of nitrogen into the deposition process which significantly improves electrical conductivity of the ITO layer. This approach is original and not commonly used for the deposition of ITO. Although, the exact explanation is not fully understood yet, it is proved by our measurements presented above. Further research, for example X-ray photoelectron spectroscopy (XPS), could reveal exact chemical stoichiometry of the films and its influence on structural formation of ITO.

Furthermore, it was shown that the HiPIMS contribution to the deposition process results in formation of larger crystal domains. More and detailed experiments, planed for a next research, could reveal how HiPIMS and RF discharges influence each other and the layer properties. Still there is room to study the effect of domain size on electrical conductivity of deposited films.

As mentioned in the Introduction the main goal of the research is development of the biosensors based on optical fibre coated by functional ITO film. Such sensors would be able to combine electrochemical measurements (enabled by the conductivity of the ITO film on the fibre surface) as well as optical spectroscopy measurements (enabled by the transparency of the ITO film and the fibre itself) in a liquid solution. For the cylindrically homogeneous layer coverage of the fibre, a rotation stage, which is based on the magnetically transferred moment, was designed and constructed in the frame of the thesis. Basic scheme of the rotation stage and its position in the deposition chamber are shown in figure 6-1. The stage was designed to be compatible with the rotation table present at the bottom of the chamber.

Figure 6-2 shows an example of covered fibres and SEM images of the layer. The upper panel shows the optical fibres in a holder after the deposition of ITO. The thinner part of each fibre is a core of the fibre without cladding and plastic coating, which serves as an active part of the sensor. The lower panel with SEM images shows that rotation stage enable direct deposition of ITO on the fibre core creating the cylindrically homogeneous layer. This work and research was also carried out in the frame of diploma thesis. However, the

functional coating of the fibres and their preliminary diagnostic results are not included in this manuscript. Optimization of ITO for the electrochemical and optical measurements using covered fibres is a subject of the further research.

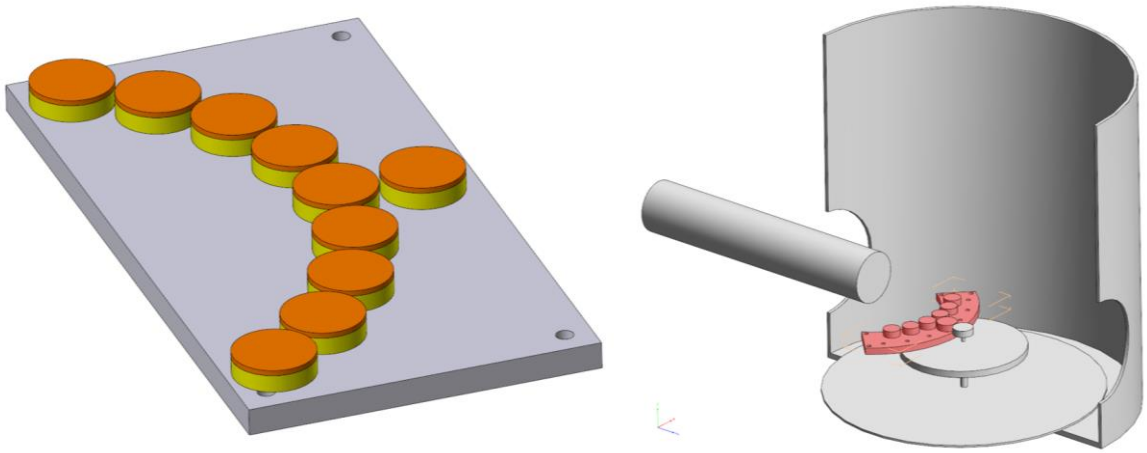

Figure 6-1 Left panel – scheme of the rotation stage. Yellow rings are made of PTFE and have inserted neodymium magnets to improve moment transfer from the rotating table. Orange are PTFE wafers cover magnets and have holes for holding of fibres. Right panel – the rotation stage (red) inside the chamber.

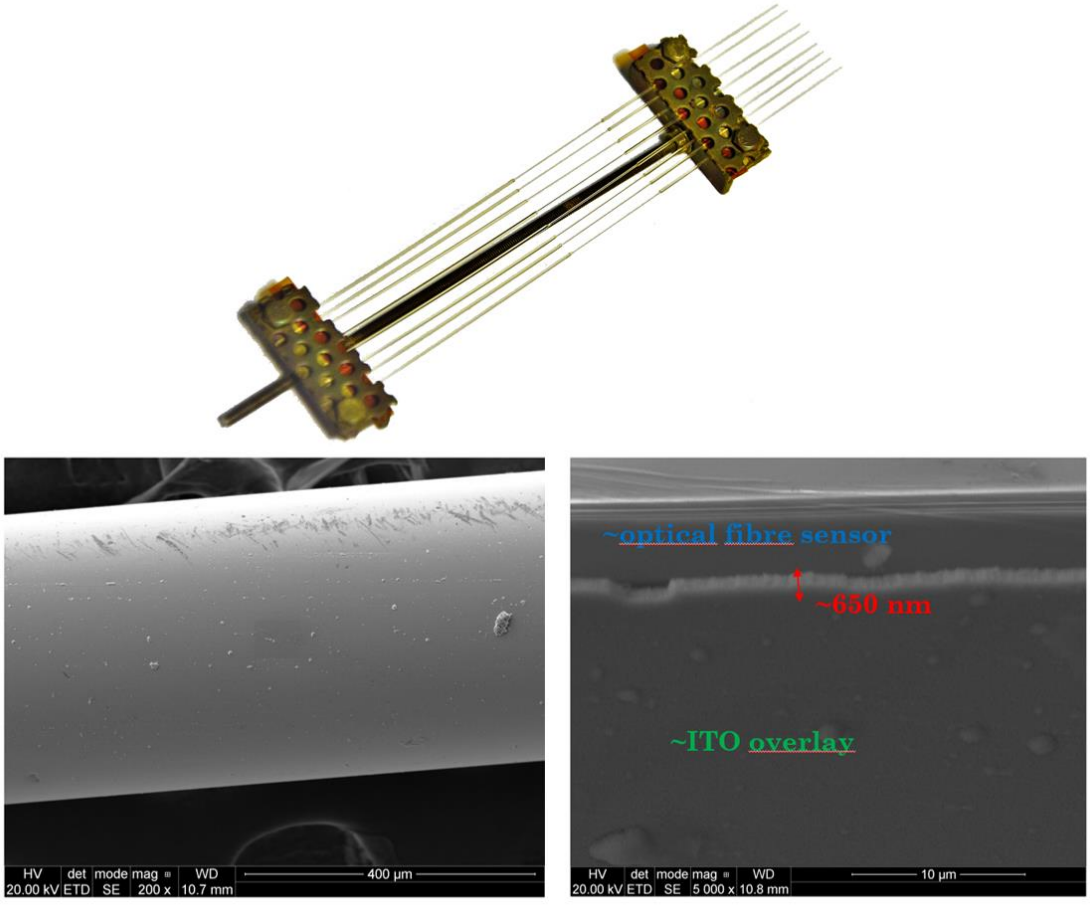

Figure 6-2 Upper panel – the optical fibres in a holder after the deposition of ITO, using the rotation stage. Lower panel – SEM images of optical fibres with deposited ITO films.

7 Reference

[1] D. M. Mattox, Handbook of Physical Vapor Deposition Processing, Oxford: Elsevier Inc., 2010.

[2] M. A. Lieberman and A. J. Lichtenberg, Principles of Plasma Discharges and Materials Processing, Hoboken, New Jersey: John Wiley & Sons, Inc., 2005.

[3] V. Martišovitš, Základy fyziky plazmy, Bratislava: Univerzita Komenského, 2004.

[4] P. M. Martin, Handbook of Deposition Technologies for Films and Coatings, Oxford: Elsevier Inc., 2005.

[5] J. Musil, J. Vlcek a P. Baroch, Materials Surface Processing by Direct Energy Techniques, Oxford: Elsevier Inc., 2006.

[6] http://www.lesker.com/ - deposition sources, materials

[7] R. Hippler, H. Kersten, M. Schmidt and K. Schoenbach, Low Temperature Plasmas: Fundamentals, Technologies and Techniques, Berlin: WILEY-VCH Verlag, 2007.

[8] J. T. Gudmundsson, N. Brenning, D. Lundin and U. Helmersson, "High power impulse magnetron sputtering discharge," *Journal of Vacuum Science & Technology*, no. 30, 2012.

[9] H. Kim, C. M. Gilmore, A. Piqué, J. S. Horwitz, H. Mattoussi, H. Murata, Z. H. Kafafi and D. B. Chrisey, "Electrical, optical, and structural properties of indium–tin–oxide thin films for organic light-emitting devices," *Journal of Applied Physics*, no. 86, 1999.

[10] P. P. Edwards, A. Porch, M. O. Jones, D. V. Morgan and R. M. Perks, "Basic materials physics of transparent conducting oxides," *Dalton Transactions*, no. 19, 2004.

[11] J. Du, X. Chen, C. Liu, J. Ni, G. Hou, Y. Zhao and X. Zhang, "Highly Transparent and Conductive Indium Tin Oxide Thin Films for Solar Cells Grown by Reactive Thermal Evaporation at Low Temperature," *Applied Physics A: Materials Science & Processing*, no. 117, 2014.

[12] V. Stranak, M. Cada, Z. Hubicka, M. Tichy and R. Hippler, "Time-resolved investigation of dual high power impulse magnetron," *Journal of Applied Physics*, no. 108, 2010.

[13] A. Shimamoto, K. Yamashita, H. Inoue, S.-m. Yang, M. Iwata and N. Ike, "A Nondestructive Evaluation Method: Measuring the Fixed Strength of Spot-Welded Joint Points by Surface Electrical Resistivity," *Journal of Pressure Vessel Technology*, no. 135, 2013.

[14] https://www2.chemistry.msu.edu/

[15] R. A. Serway, R. J. Beichner and J. W. Jewett, Physics for Scientists and Engineers, Boston: Cengage Learning, 2013.

[16] J. Meichsner, M. Schmidt, R. Schneider and H.-E. Wagner, Nonthermal Plasma Chemistry and Physics, Boca Raton: Taylor & Francis Group, 2013.